Modeling Photonic Crystal Band Structures Using Hermite FEM

A Major Qualifying Project report
submitted to the faculty of
WORCESTER POLYTECHNIC INSTITUTE
in partial fulfillment of the requirements
for the Degree of Bachelor of Science
by

Christopher Boucher

Physics Department, Worcester Polytechnic Institute,
Worcester, MA 01609, USA

Submitted: June 8, 2012

Approved:

L. Ramdas Ram-Mohan, Advisor

Abstract

Maxwell's vector field equations represent significant challenges for the numerical solution of electric and magnetic fields in complex geometries. With increasing complexity in the design of electromagnetic devices as in automobiles, metamaterials, and optical interconnects, it becomes imperative to develop compact algorithms for electrodynamic calculations that will generate high accuracy with minimal computational time. We solve the field equations for the example of a two-dimensional photonic crystal using the finite element method with Hermite interpolation polynomials. We demonstrate that the Hermite interpolation polynomials, due to their derivative continuity across elements, yield accurate predictions of the fields in a photonic crystal at a much lower computational cost than conventional approaches to this problem.

Contents

List of Figures

List of Tables

Chapter 1

Introduction

Electrodynamic devices of ever increasing complexity are being employed in a wide variety of industries. The design of modern automobiles includes electromagnetic components whose behavior in isolation and in combination as aggregates requires a significant amount of modeling and simulation. At the nanoscale, similar circumstances are faced for optical interconnects, quantum well laser design, and in plasmonics. Again, reliable simulations are essential to ensure that each device does not affect others near it through electromagnetic cross-talk. The novel effects exhibited by metamaterials containing negative refractive index components are all simulated before being assembled in order to optimize their optical properties as desired.

Present-day computational electrodynamic modeling relies heavily on finite element, finite difference, and spectral methodologies. Here we focus on a scalar finite element approach in which the field components are approximated as local polynomials over discrete subdomains. We show that the use of $\mathcal{C}_1$-continuous Hermite interpolation polynomials on triangular elements provide very accurate solutions with a minimal number of elements used in the discretization.

In this report, we show that the use of Hermite interpolation polynomials, which are scalar fifth-order polynomials in two dimensions, provide an accurate means of predicting the properties of two-dimensional photonic crystals at a small fraction of the computational cost of more popular techniques, particularly plane-wave expansions. The plane-wave expansion technique is a Fourier expansion of the real space vector fields that approximates the elec-

tric and magnetic fields as linear combinations of a large number of plane waves. Typical calculations require 10^5 to 10^6 plane waves to provide converged results, using fully occupied matrices of such dimensions. The finite element approach leads to sparse occupancy (less than 0.2%) of matrices due to the local connectivity of elements, and to matrix sizes on the order of 10^4 to 10^5 for similar levels of accuracy. The photonic wavefunctions and frequency dispersion surfaces are shown for several transverse electric (TE) and transverse magnetic (TM) modes. We also present a group-theoretic analysis of energy bands, their wavefunctions and their degeneracies.

1.1 Fundamentals of Hermite Interpolation

We propose the use of an alternative set of polynomial basis functions, the scalar fifth-order Hermite interpolation polynomials, [1–4] for the numerical calculations of electromagnetic fields. As scalar functions, these polynomials interpolate data which is stored in the nodes of a finite element mesh. The defining characteristic of Hermite polynomials in general is that they store information about a function as well as its derivatives at the nodes of the elements. By expressing an unknown function as a linear combination of Hermite polynomials, one may use the Finite Element Method to guarantee the continuity of a function and one or more of its derivatives across interelement boundaries, ensuring that the solution is smooth and increasing the rate at which numerical error decays with increased mesh refinement.

Recent work by Kassebaum at al. [5] has demonstrated that Hermite interpolation polynomials can be derived for a particular finite element and a desired order of derivative continuity using group representation theory. [6] The interpolation polynomials generated using a group theory analysis [5] are distinct from previous sets of Hermite polynomials which were defined for the same type of element and the same order of derivative continuity, but were calculated using ad hoc methods. [4] However, the approach based on group theory has the potential to generate $\mathcal{C}_n$-continuous Hermite interpolation polynomials for varying dimensions and values of n, which represents the highest derivative order which is continuous across elements. Traditional Lagrange interpolation functions are $\mathcal{C}_0$, while the Hermite functions used in this study are $\mathcal{C}_1$.

The choice of a set of interpolation polynomials fundamentally determines the accuracy of the FEM. By imposing the continuity of one or more of the derivatives of the piecewise functions as well as the functions themselves, one may considerably improve the convergence rate of the method. The use of $\mathcal{C}_1$-continuous Hermite interpolation polynomials has led to impressive success in other areas of physics, such as quantum mechanics. [1] Hermite polynomials have also been used successfully to simulate fields in a conducting waveguide. [7, 8] These Hermite interpolation polynomials are given in Table 1.1.

The advantage of a $\mathcal{C}_1$-continuous polynomial basis is that it naturally

conforms to the smooth behavior of most physically realizable functions and their derivatives. In addition, the allocation of separate rows and columns of the element matrices for derivative data offers a convenient means of imposing Dirichlet, Neumann, or mixed boundary conditions. The basis used throughout this work is an incomplete set of fifth-order polynomials, guaranteeing the continuity of a function and its gradient across interelement boundaries. The polynomial functions are shown in Fig. 1.1.

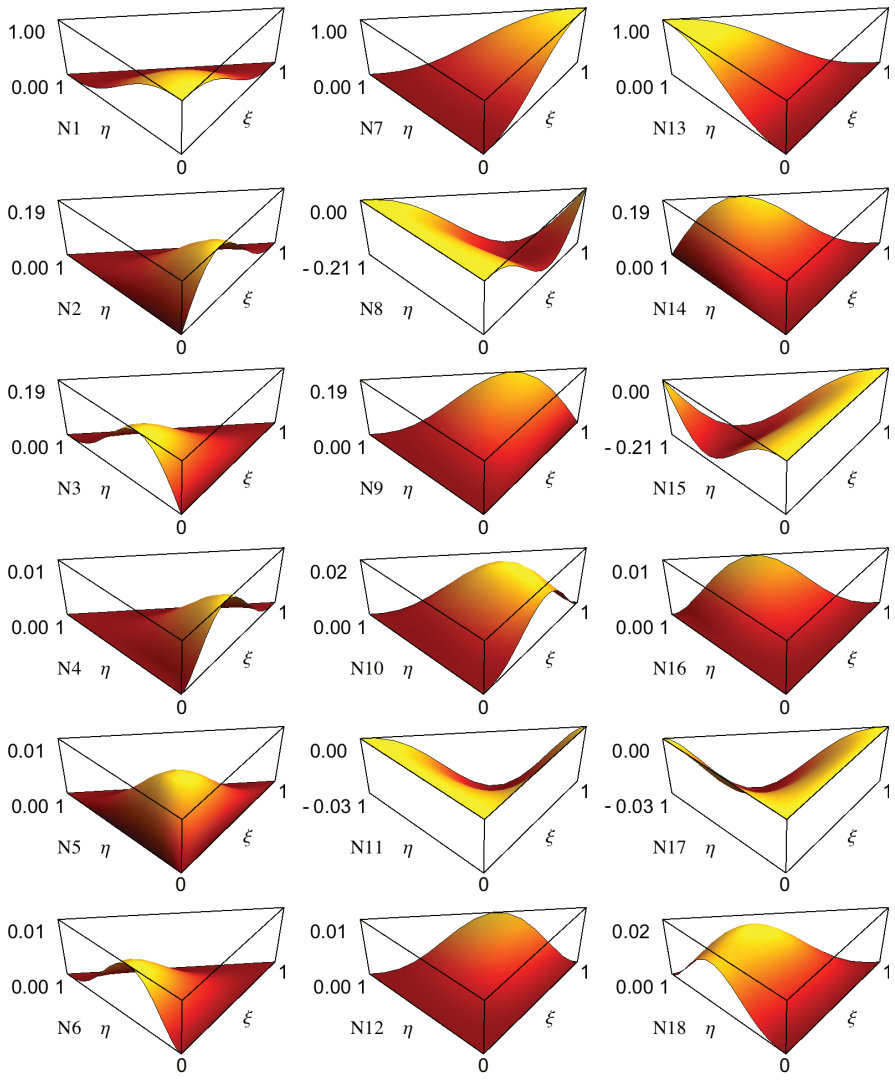

Figure 1.1: The Hermite interpolation polynomials are plotted on the standard right triangle. Each node has six degrees of freedom corresponding to the function and including up to the second derivatives. Coefficients of functions N_1, N_7, and N_{13} correspond to the function values at the nodes. Coefficients of functions $N_2, N_3, N_8, N_9, N_{14}$, and N_{15} correspond to the first derivative values at the nodes. The rest are associated with second derivative degrees of freedom.

Table 1.1: The set of 5th-order, C_1-continuous Hermite shape functions for the triangle are tabulated. The local coordinates of the right triangle are ξ and η, and we use $\sigma = 1 - \xi - \eta$ to simplify the expressions for the polynomials.. The shape functions are arranged so that the six functions for each node correspond to $f, f_x, f_y, f_{xx}, f_{xy}$, and f_{yy}, respectively. The functions were obtained from Ram-Mohan [1, p.227]; the concept of an incomplete C_1-continuous, two-dimensional, fifth-order Hermite polynomial set can be dated back to Bell [2] and Argyris. [3]

Node	Shape function
	$N_1 = \sigma^2 (10\sigma - 15\sigma^2 + 6\sigma^3 + 30\xi\eta (\xi + \eta))$
	$N_2 = \xi\sigma^2 (3 - 2\sigma - 3\xi^2 + 6\xi\eta)$
Node 1	$N_3 = \eta\sigma^2 (3 - 2\sigma - 3\eta^2 + 6\xi\eta)$
$(0,0)$	$N_4 = \xi^2\sigma^2 (1 - \xi + 2\eta)/2$
	$N_5 = \xi\eta\sigma^2$
	$N_6 = \eta^2\sigma^2 (1 + 2\xi - \eta)/2$
	$N_7 = \xi^2 (10\xi - 15\xi^2 + 6\xi^3 + 15\eta^2\sigma)$
	$N_8 = \xi^2 (-8\xi + 14\xi^2 - 6\xi^3 - 15\eta^2\sigma)/2$
Node 2	$N_9 = \xi^2\eta (6 - 4\xi - 3\eta - 3\eta^2 + 3\xi\eta)/2$
$(1,0)$	$N_{10} = \xi^2 \left(2\xi (1 - \xi)^2 + 5\eta^2\sigma\right)/4$
	$N_{11} = \xi^2\eta (-2 + 2\xi + \eta + \eta^2 - \xi\eta)/2$
	$N_{12} = \frac{1}{4}\xi^2\eta^2\sigma + \frac{1}{2}\xi^3\eta^2$
	$N_{13} = \eta^2 (10\eta - 15\eta^2 + 6\eta^3 + 15\xi^2\sigma)$
	$N_{14} = \eta^2\xi (6 - 4\eta - 3\xi - 3\xi^2 + 3\eta\xi)/2$
Node 3	$N_{15} = \eta^2 (-8\eta + 14\eta^2 - 6\eta^3 - 15\xi^2\sigma)/2$
$(0,1)$	$N_{16} = \frac{1}{4}\eta^2\xi^2\sigma + \frac{1}{2}\eta^3\xi^2$
	$N_{17} = \eta^2\xi (-2 + 2\eta + \xi + \xi^2 - \eta\xi)/2$
	$N_{18} = \eta^2 \left(2\eta (1 - \eta)^2 + 5\xi^2\sigma\right)/4$

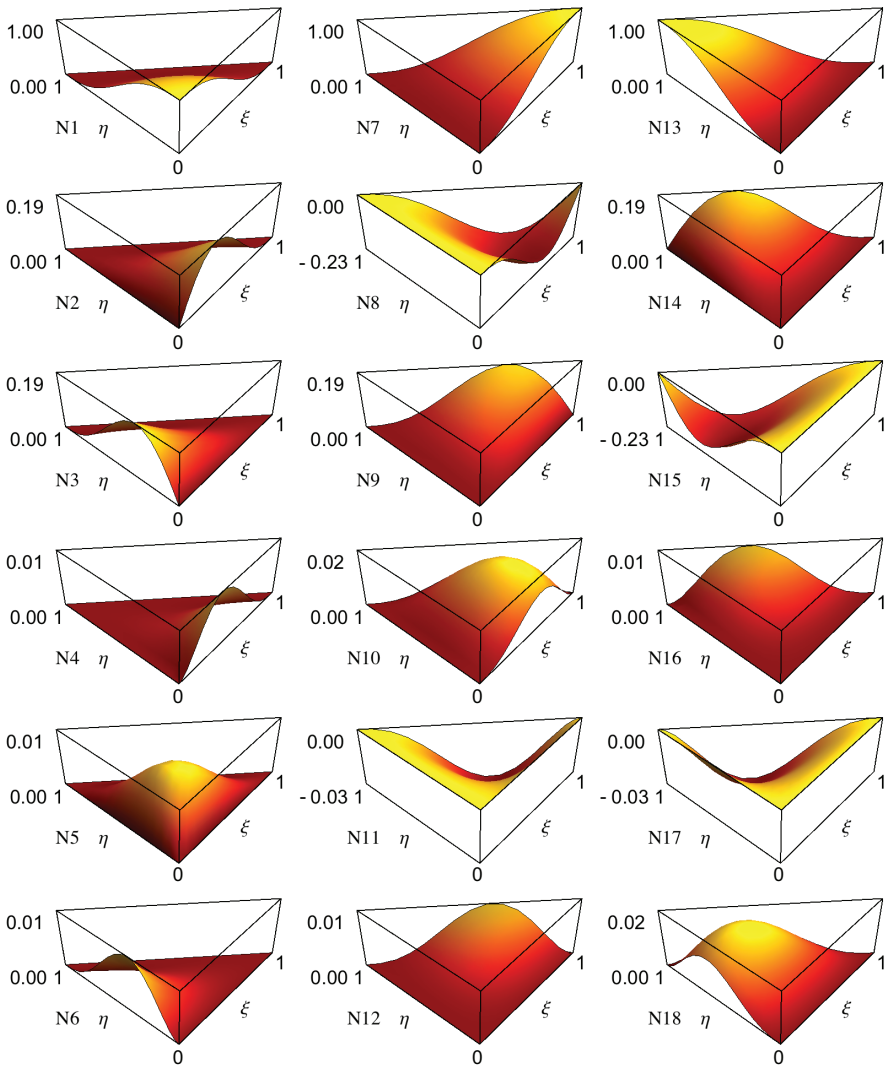

Figure 1.2: The Hermite interpolation polynomials derived by Kassebaum et al. [5] are plotted on the standard right triangle. While the polynomials are similar in shape to those given by Bell as shown in Fig. 1.1, the polynomials shown here have the advantage of being derived directly from continuity requirements and group representation theory, providing a systematic means of extending the derivation of Hermite polynomials to higher dimensions or higher orders of continuity.

Table 1.2: Quintic Hermite interpolation polynomials derived in the equilateral triangular reference element that support $C^{(1)}$ continuous quartic polynomials across shared sides of elements mapped into the right triangle. These polynomials were derived using group representation theory. [5]

Node	Shape function
	$N_1 = (1-\xi-\eta)^2(3\xi^2(1-\eta)-6\xi^3+\xi(2+3(2-\eta)\eta)+(1-\eta)(1+3\eta+6\eta^2))$.
	$N_2 = \frac{1}{2}\xi(1-\xi-\eta)^2(2+4\eta+\xi(4-6\xi-3\eta))$.
Node 1	$N_3 = \frac{1}{2}\eta(1-\xi-\eta)^2(\xi(4-3\eta)+2(1-\eta)(1+3\eta))$.
$(0,0)$	$N_4 = \frac{1}{4}\xi^2(1-\xi-\eta)^2(2-2\xi-\eta)$.
	$N_5 = \xi\eta(1-\xi-\eta)^2$.
	$N_6 = \frac{1}{4}\eta^2(1-\xi-\eta)^2(2-2\eta-\xi)$.
	$N_7 = \xi^2(\xi(10-3\xi(5-2\xi))+15(1-\xi)^2\eta-15(1-\xi)\eta^2)$.
	$N_8 = \frac{1}{2}\xi^2(1-\xi)(6\xi^2-15(1-\eta)\eta-\xi(8-15\eta))$.
Node 2	$N_9 = \frac{1}{2}\xi^2\eta(\xi(3\eta-4)+3(2-\eta-\eta^2))$.
$(1,0)$	$N_{10} = \frac{1}{4}\xi^2(\xi-1)(2(\xi-1)\xi-5(1-\xi)\eta+5\eta^2)$.
	$N_{11} = \frac{1}{2}\xi^2\eta(\eta^2+\eta+\xi(2-\eta)-2)$.
	$N_{12} = \frac{1}{4}\xi^2(1+\xi-\eta)\eta^2$.
	$N_{13} = \eta^2(15\xi^2(\eta-1)+15\xi(1-\eta)^2+\eta(10-3\eta(5-2\eta)))$.
	$N_{14} = \frac{1}{2}\xi\eta^2(6-3\xi(1+\xi-\eta)-4\eta)$.
Node 3	$N_{15} = \frac{1}{2}\eta^2(1-\eta)(15(\xi-1)\xi-(8-15\xi)\eta+6\eta^2)$.
$(0,1)$	$N_{16} = \frac{1}{4}\xi^2\eta^2(1-\xi+\eta)$.
	$N_{17} = \frac{1}{2}\xi\eta^2(\xi+\xi^2+2\eta-\xi\eta-2)$.
	$N_{18} = \frac{1}{4}\eta^2(\eta-1)(5\xi^2-5\xi(1-\eta)-2(1-\eta)\eta)$.

Chapter 2

Photonic Crystal Analysis

We now consider two-dimensional photonic crystals and their band structures. A photonic crystal is a periodic arrangement of materials of different dielectric properties that only permits electromagnetic waves of certain frequencies and polarizations to propagate. Their design through the geometric placement of the dielectrics provides a level of control over the dispersion relations satisfied by photons in the array.

The first proposals for the design of photonic crystals were independently made by Yablonovitch [9] and by John. [10] The foundations for the study of propagating modes in a photonic crystal, including Maxwell's equations and Bloch's theorem, were well in place prior to the mid-1900s. [11] However, the first modern treatment of a periodic array of dielectric materials can be traced back to Ohtaka in 1979. [12–15] Since then, rapid increases in computing power have led to the expansion of opportunities for further modeling of periodic dielectric arrangements. With mastery of the design and machining of photonic crystals comes the ability to design a wide variety of optoelectronic devices including low-loss reflecting surfaces, waveguides, filters, flat lenses, optical inter-connects, etc., making the efficient prediction of crystal properties a high priority for physicists and engineers. [11, 16, 17]

By assuming that the photonic crystal contains an arbitrarily large number of unit cells, one may use Bloch's theorem [18] (also known as Floquet's theorem), [19, 20] to decompose the electric or magnetic field into the product of a periodic function, or cell function, and a plane wave, or envelope function. Currently the most popular means of computing the band struc-

ture (i.e., frequency versus wavevector plot) of a photonic crystal is to represent the cell function itself as a linear combination of plane waves. [15–17] However, the approach outlined in the following is to use the finite element method (FEM) with Hermite interpolation polynomials. The same polynomials have already been shown to exhibit high accuracy and reliable performance when implemented to solve quantum mechanical problems. [1] The derivation of an action integral for the magnetic field in a photonic crystal is discussed in the next section.

2.1 Theory of Photonic Crystals

We utilize the finite element method to predict the characteristics of a two-dimensional photonic crystal. Such a crystal consists of multiple dielectric materials arranged periodically in two directions, with homogeneous characteristics in the third direction. In this section, we use Maxwell's Equations and the periodicity of the dielectric structure to construct an action integral to be minimized using the Hermite FEM.

2.1.1 Derivation of the action integral

We seek to calculate the band structure and vector fields in a photonic crystal by expressing the field components as piecewise-continuous Hermite polynomials on an unstructured finite element grid and applying the principle of stationary action [1] to an equation of motion derived from Maxwell's equations. We begin with Maxwell's equations [21] expressed in MKS units,

$$\nabla \cdot \mathbf{D} = \rho, \tag{2.1}$$

$$\nabla \times \mathbf{H} - \frac{\partial \mathbf{D}}{\partial t} = \mathbf{J}, \tag{2.2}$$

$$\nabla \times \mathbf{E} + \frac{\partial \mathbf{B}}{\partial t} = 0, \tag{2.3}$$

$$\nabla \cdot \mathbf{B} = 0. \tag{2.4}$$

In the above, we express the electric displacement $\mathbf{D}$ and the magnetic induction $\mathbf{B}$ in terms of the electric and magnetic fields $\mathbf{E}$ and $\mathbf{H}$,

$$\mathbf{D} = \epsilon \mathbf{E}; \qquad \mathbf{B} = \mu \mathbf{H}. \tag{2.5}$$

If the medium is isotropic, ϵ and μ are scalar quantities, while in general they behave as second-rank tensors. Let us define the dimensionless quantities ϵ_r and μ_r so that

$$\epsilon = \epsilon_r \epsilon_0, \qquad \mu = \mu_r \mu_0 \tag{2.6}$$

with ϵ_0 and μ_0 being the permittivity and permeability of free space, respectively.

We assume that the photonic crystal is charge-free and current-free. We also assume that the fields are time-harmonic so that $\mathbf{H}(\mathbf{r}, t) = \mathbf{H}(\mathbf{r}) \exp(-i\omega t)$ and $\mathbf{E}(\mathbf{r}, t) = \mathbf{E}(\mathbf{r}) \exp(-i\omega t)$, where $\omega = k_0 c$ is the frequency of the electromagnetic wave. With these assumptions we can use Eqs. (2.2-2.3) to construct the double-curl form of Maxwell's equations,

$$\nabla \times \left(\frac{1}{\epsilon_r} \nabla \times \mathbf{H} \right) - k_0^2 \mu_r \mathbf{H} = 0, \tag{2.7}$$

which only includes the spatial dependence of the $\mathbf{H}$-field. Alternatively, the double-curl form may be written in terms of the electric field,

$$\nabla \times \left(\frac{1}{\mu_r} \nabla \times \mathbf{E} \right) - k_0^2 \epsilon_r \mathbf{E} = 0. \tag{2.8}$$

We use Eq. (2.7) to construct the action integral. First, we multiply by a variation with respect to the conjugate field, $\delta \mathbf{H}^*$, and integrate to obtain

$$\int_V d^3 r \, \delta \mathbf{H}^* \cdot \left[\nabla \times \left(\frac{1}{\epsilon_r} \nabla \times \mathbf{H} \right) - k_0^2 \mu_r \mathbf{H} \right] = 0. \tag{2.9}$$

Because the photonic crystal is two-dimensional and has homogeneous properties in the third direction, we can eliminate the integration in the direction in which the crystal has homogeneous properties. We assume that the remaining two integrations are performed over a single unit cell of the photonic crystal, and refer to this two-dimensional domain as Ω. In this manner Eq. (2.9) becomes

$$\int_\Omega d^2 r \, \delta \mathbf{H}^* \cdot \left[\nabla \times \left(\frac{1}{\epsilon_r} \nabla \times \mathbf{H} \right) - k_0^2 \mu_r \mathbf{H} \right] = 0. \tag{2.10}$$

We now apply the principle of stationary action to Eq. (2.10). In the following derivation we employ the vector identity

$$\begin{aligned} \nabla \cdot (\mathbf{P} \times \mathbf{R}) &= \epsilon_{ijk} \left(\partial_i P_j\right) R_k - P_j \epsilon_{jik} \partial_i R_k \\ &= (\nabla \times \mathbf{P}) \cdot \mathbf{R} - \mathbf{P} \cdot (\nabla \times \mathbf{R}) \,, \end{aligned} \tag{2.11}$$

where ϵ_{ijk} is the Levi-Civita tensor. Now let $\mathbf{R} = \epsilon_r^{-1} \nabla \times \mathbf{H}$ and $\mathbf{P} = \delta \mathbf{H}^*$. Then from Eq. (2.11),

$$\begin{aligned} \nabla \cdot \left[\delta \mathbf{H}^* \times \left(\frac{1}{\epsilon_r} \nabla \times \mathbf{H} \right) \right] &= (\nabla \times \delta \mathbf{H}^*) \cdot \left(\frac{1}{\epsilon_r} \nabla \times \mathbf{H} \right) \\ &\quad - \delta \mathbf{H}^* \cdot \left[\nabla \times \left(\frac{1}{\epsilon_r} \nabla \times \mathbf{H} \right) \right] . \end{aligned} \tag{2.12}$$

This leads to the integrals

$$\begin{aligned} \int_\Omega d^2 r \nabla \cdot \left[\delta \mathbf{H}^* \times \left(\frac{1}{\epsilon_r} \nabla \times \mathbf{H} \right) \right] &= \int_\Omega d^2 r \, (\nabla \times \delta \mathbf{H}^*) \cdot \left(\frac{1}{\epsilon_r} \nabla \times \mathbf{H} \right) \\ &\quad - \int_\Omega d^2 r \delta \mathbf{H}^* \cdot \left[\nabla \times \left(\frac{1}{\epsilon_r} \nabla \times \mathbf{H} \right) \right] . \end{aligned} \tag{2.13}$$

The left side can be reduced to a surface integral by Gauss's Theorem, yielding a line integral about the perimeter of the unit cell. Rearrangement of Eq. (2.13) then yields

$$\begin{aligned} \int_\Omega d^3 r \, \delta \mathbf{H}^* \cdot \left[\nabla \times \left(\frac{1}{\epsilon_r} \nabla \times \mathbf{H} \right) \right] &= \int_\Omega d^3 r \, (\nabla \times \delta \mathbf{H}^*) \cdot \left(\frac{1}{\epsilon_r} \nabla \times \mathbf{H} \right) \\ &\quad - \oint_\Gamma ds \, \hat{\mathbf{n}} \cdot \left[\delta \mathbf{H}^* \times \left(\frac{1}{\epsilon_r} \nabla \times \mathbf{H} \right) \right] . \end{aligned} \tag{2.14}$$

By Eq. (2.14) we see that the integral of the double curl can be expressed in an alternative form which does not have second derivative terms. Limiting the action to first-derivative terms is a desirable outcome because the interpolation polynomials used to calculate the eigenvalues are only $\mathcal{C}_1$-continuous. In the following section we introduce the Bloch-Floquet theorem, apply it to the fields in a photonic crystal, and use it to prove that the surface term in Eq. (2.14) equals zero.

2.1.2 Application of Bloch's Theorem

By the Bloch-Floquet Theorem, [18–20], we can decompose the magnetic field into two terms,

$$\mathbf{H}(\mathbf{r}) = \mathbf{U}(\mathbf{r})\, e^{i\mathbf{q}\cdot\mathbf{r}}. \tag{2.15}$$

We refer to the first term, $\mathbf{U}$, as the **cell function**. We call the exponential term the **envelope function**. In the examples treated in this report, in which the unit cell is a rectangle of dimensions $d_x \times d_y$, the vector $\mathbf{q}$ can be expressed as

$$\mathbf{q} = \frac{\pi q_x}{d_x}\hat{\mathbf{i}} + \frac{\pi q_y}{d_y}\hat{\mathbf{j}} + 0\hat{\mathbf{k}}, \tag{2.16}$$

in which the range of q_x and q_y values which comprise the Brillouin zone [22] are

$$-1 < q_x \leq 1, \qquad -1 < q_y \leq 1. \tag{2.17}$$

Values of q_x and q_y outside of the ranges defined in Eq. (2.17) are redundant. The cell function obeys periodic boundary conditions over a single unit cell. By applying the decomposition in Eq. (2.15) to the surface term in Eq. (2.14), we express the line integral as

$$\begin{aligned}\oint_\Gamma ds\, \hat{\mathbf{n}} \cdot \left[\delta\mathbf{H}^* \times \left(\frac{1}{\epsilon_r}\nabla \times \mathbf{H}\right)\right] &= \delta \oint_\Gamma ds\, \hat{\mathbf{n}} \cdot \left[\mathbf{H}^* \times \left(\frac{1}{\epsilon_r}\nabla \times \mathbf{H}\right)\right] \\ &= \delta \oint_\Gamma ds \hat{\mathbf{n}} \cdot \left[\left(\mathbf{U}^* e^{-i\mathbf{q}\cdot\mathbf{r}}\right) \times \left(\frac{1}{\epsilon_r}\nabla \times \left(\mathbf{U} e^{i\mathbf{q}\cdot\mathbf{r}}\right)\right)\right].\end{aligned} \tag{2.18}$$

We expand the curl term in Eq. (2.18) as

$$\begin{aligned}\nabla \times \left(\mathbf{U} e^{i\mathbf{q}\cdot\mathbf{r}}\right) &= e^{i\mathbf{q}\cdot\mathbf{r}}\left(\nabla \times \mathbf{U}\right) + \left(\nabla e^{i\mathbf{q}\cdot\mathbf{r}}\right) \times \mathbf{U} \\ &= e^{i\mathbf{q}\cdot\mathbf{r}}\left(\nabla \times \mathbf{U}\right) + e^{i\mathbf{q}\cdot\mathbf{r}}\left(i\mathbf{q} \times \mathbf{U}\right).\end{aligned} \tag{2.19}$$

The factors of $\exp(i\mathbf{q}\cdot\mathbf{r})$ and $\exp(-i\mathbf{q}\cdot\mathbf{r})$ in Eq. (2.18) cancel each other, reducing the surface integral to

$$\delta \oint_\Gamma ds\, \hat{\mathbf{n}} \cdot \left[\mathbf{U}^* \times \frac{1}{\epsilon_r}\left(\nabla \times \mathbf{U} + i\mathbf{q} \times \mathbf{U}\right)\right]. \tag{2.20}$$

Because $\mathbf{U}$ and ϵ_r are both periodic, for every point on the boundary of the unit cell there will be a point on the opposite side of the cell with the same

values of $\mathbf{U}$ and ϵ_r, but with $\hat{\mathbf{n}}$ pointing in the opposite direction. Therefore it is clear that the line integral given in Eq. (2.20) is exactly zero. We now apply this conclusion and Eq. (2.14) to Eq. (2.10) to obtain a new expression for the action integral:

$$\int_\Omega d^2r \left[(\nabla \times \delta\mathbf{H}^*) \cdot \frac{1}{\epsilon_r} \cdot (\nabla \times \mathbf{H}) - \delta\mathbf{H}^* \cdot k_0^2 \mu_r \cdot \mathbf{H} \right] = 0, \tag{2.21}$$

which may be expressed as

$$\delta\mathcal{A} = \delta \int_\Omega d^2r \left[(\nabla \times \mathbf{H}^*) \cdot \frac{1}{\epsilon_r} \cdot (\nabla \times \mathbf{H}) - \mathbf{H}^* \cdot k_0^2 \mu_r \cdot \mathbf{H} \right] = 0. \tag{2.22}$$

In Eq. (2.22) we see the principle of least action applied to Maxwell's vector equations. We conclude that the action integral is defined as

$$\mathcal{A} = \int_\Omega d^2r \left[(\nabla \times \mathbf{H}^*) \cdot \frac{1}{\epsilon_r} \cdot (\nabla \times \mathbf{H}) - \mathbf{H}^* \cdot k_0^2 \mu_r \cdot \mathbf{H} \right], \tag{2.23}$$

in which the integration is performed over one unit cell of the two-dimensional photonic crystal. Alternatively we may begin the derivation of the action integral by using the electric field instead of the magnetic field. In this case we again use the Bloch-Floquet Theorem to separate the field into a cell function $\mathbf{U}$ and an envelope function, and see that the surface term arising from Gauss's Theorem is still zero. The resulting action is

$$\mathcal{A} = \int_\Omega d^2r \left[(\nabla \times \mathbf{E}^*) \cdot \frac{1}{\mu_r} \cdot (\nabla \times \mathbf{E}) - \mathbf{E}^* \cdot k_0^2 \epsilon_r \cdot \mathbf{E} \right]. \tag{2.24}$$

In the following section we use the Bloch-Floquet theorem to simplify the action by classifying all possible solutions into two distinct types of modes.

2.1.3 Classification of TE- and TM-modes

We begin by decomposing each term of Eq. (2.23) into cell functions and envelope functions. The second term of the integral simply reduces to

$$\mathbf{H}^* \cdot k_0^2 \mu_r \cdot \mathbf{H} = e^{-i\mathbf{q}\cdot\mathbf{r}} \mathbf{U}^* \cdot k_0^2 \mu_r \cdot e^{i\mathbf{q}\cdot\mathbf{r}} \mathbf{U} = \mathbf{U}^* \cdot k_0^2 \mu_r \cdot \mathbf{U}. \tag{2.25}$$

In Eq. (2.19) we have already shown how the curl of $\mathbf{H}$ can be expressed in terms of the cell function and envelope function. Writing this explicitly in matrix form, we obtain

$$\nabla \times \mathbf{H} = e^{i\mathbf{q}\cdot\mathbf{r}} \left[\begin{pmatrix} \partial_y U_z - \partial_z U_y \\ \partial_z U_x - \partial_x U_z \\ \partial_x U_y - \partial_y U_x \end{pmatrix} + i \begin{pmatrix} 2\pi q_y U_z/d_y \\ -2\pi q_x U_z/d_x \\ 2\pi q_x U_y/d_x - 2\pi q_y U_x/d_y \end{pmatrix} \right]. \quad (2.26)$$

Eq. (2.26) may be simplified by classifying all possible solutions into two distinct cases:

Transverse electric (TE) modes: $E_z = 0$, $H_x = H_y = 0$, and all other vector components are nonzero.

Transverse magnetic (TM) modes: $E_x = E_y = 0$, $H_z = 0$, and all other vector components are nonzero.

Any possible field in the two-dimensional photonic crystal may be expressed as a combination of TE- and TM-modes. Therefore, if certain frequencies of electromagnetic waves are absent from the band structures of both TE- and TM-modes, then those frequencies are not transmitted by the photonic crystal.

In a transverse electric (TE) mode, the periodic cell function $\mathbf{U}$ only has a nonzero component in the z-direction, $U_z(x, y)$, so the magnetic field $\mathbf{H}$ is polarized in the z-direction. Then Eq. (2.26) may be reduced to

$$\nabla \times \mathbf{H} = e^{i\mathbf{q}\cdot\mathbf{r}} \begin{pmatrix} \partial_y U_z + \pi i q_y U_z/d_y \\ -\partial_x U_z - \pi i q_x U_z/d_x \\ 0 \end{pmatrix}, \quad (2.27)$$

and the complex conjugate yields

$$\nabla \times \mathbf{H}^* = e^{-i\mathbf{q}\cdot\mathbf{r}} \begin{pmatrix} \partial_y U_z - \pi i q_y U_z/d_y \\ -\partial_x U_z + \pi i q_x U_z/d_x \\ 0 \end{pmatrix}. \quad (2.28)$$

Assuming the dielectric is isotropic, we may treat the relative permittivity and permeability as scalar quantities and express the product of two curls as

$$(\nabla \times \mathbf{H}^*) \cdot \frac{1}{\epsilon_r} \cdot (\nabla \times \mathbf{H}) = \left(U_z^*\right) \mathbf{A} \frac{1}{\epsilon_r} \mathbf{B} \left(U_z\right), \quad (2.29)$$

where

$$\mathbf{A} = \left(\overleftarrow{\partial_y} - \frac{\pi i q_y}{d_y}, \quad -\overleftarrow{\partial_x} + \frac{\pi i q_x}{d_x} \right), \qquad \mathbf{B} = \begin{pmatrix} \overrightarrow{\partial_y} + \dfrac{\pi i q_y}{d_y} \\ \\ -\overrightarrow{\partial_x} - \dfrac{\pi i q_x}{d_x} \end{pmatrix}. \tag{2.30}$$

The action then simplifies to

$$\boxed{\mathcal{A} = \int_\Omega d^2 r \left[U_z^* \mathbf{A} \frac{1}{\epsilon_r} \mathbf{B} U_z - U_z^* k_0^2 \mu_r U_z \right].} \tag{2.31}$$

In the other special case, the TM mode, the polarization of the magnetic field is confined to the xy-plane, and the electric field is oriented only in the z-direction. To reduce the finite element problem to a scalar problem, it is convenient to express the Lagrangian density in terms of the electric displacement, $\mathbf{D}$. The electric displacement is a better choice than the electric field, $\mathbf{E}$, due to the continuity of the former across interfaces between dielectric materials. The in-plane components of the magnetic field may also be used to construct an action integral, but this would require a coupled set of equations involving two vector components instead of one. Recall that the action can be expressed in terms of the electric field,

$$\mathcal{A} = \int_\Omega d^2 r \left[(\nabla \times \mathbf{E}^*) \cdot \frac{1}{\mu_r} \cdot (\nabla \times \mathbf{E}) - \mathbf{E}^* \cdot k_0^2 \epsilon_r \cdot \mathbf{E} \right]. \tag{2.24}$$

Because the electric displacement is $\mathbf{D}{=}\epsilon_0 \epsilon_r \mathbf{E}$, Eq. (2.24) can be expressed as

$$\mathcal{A} = \int_\Omega d^2 r \left[\left(\nabla \times \left(\frac{1}{\epsilon_r} \mathbf{D}^* \right) \right) \cdot \frac{1}{\mu_r} \cdot \left(\nabla \times \left(\frac{1}{\epsilon_r} \mathbf{D} \right) \right) - \frac{1}{\epsilon_r} \mathbf{D}^* \cdot k_0^2 \mathbf{D} \right]. \tag{2.32}$$

The curl operation can be rewritten as

$$\nabla \times \left(\frac{1}{\epsilon_r} \mathbf{D} \right) = \nabla \left(\frac{1}{\epsilon_r} \right) \times \mathbf{D} + \frac{1}{\epsilon_r} (\nabla \times \mathbf{D}). \tag{2.33}$$

We then decompose $\mathbf{D}$ into a periodic cell function and an enveloping plane wave, as we have done for $\mathbf{H}$. Furthermore, since only TM modes are being considered, the cell function only has a z-component. We express $\mathbf{D}$ as

$$\mathbf{D} = e^{i\mathbf{q}\cdot\mathbf{r}} \bar{\mathbf{U}} = e^{i\mathbf{q}\cdot\mathbf{r}} \left(0\hat{\mathbf{i}} + 0\hat{\mathbf{j}} + \bar{U}_z \hat{\mathbf{k}} \right). \tag{2.34}$$

We can then express Eq. (2.33) as

$$\nabla\times\left(\frac{1}{\epsilon_r}\mathbf{D}\right)=\left(\nabla\frac{1}{\epsilon_r}\right)\times e^{i\mathbf{q}\cdot\mathbf{r}}\bar{\mathbf{U}}+i\mathbf{q}\times\left(\frac{1}{\epsilon_r}e^{i\mathbf{q}\cdot\mathbf{r}}\bar{\mathbf{U}}\right)+\frac{1}{\epsilon_r}e^{i\mathbf{q}\cdot\mathbf{r}}\left(\nabla\times\bar{\mathbf{U}}\right). \quad (2.35)$$

Since $\bar{\mathbf{U}}=\bar{U}_z\hat{\mathbf{k}}$, we may expand the curl operators in Eq. (2.35) to obtain

$$\nabla\times\left(\frac{1}{\epsilon_r}\mathbf{D}\right)=\begin{bmatrix}\partial_y\left(\frac{1}{\epsilon_r}\right)e^{i\mathbf{q}\cdot\mathbf{r}}\bar{U}_z+\frac{\pi i q_y}{d_y\epsilon_r}e^{i\mathbf{q}\cdot\mathbf{r}}\bar{U}_z+\frac{1}{\epsilon_r}e^{i\mathbf{q}\cdot\mathbf{r}}\partial_y\bar{U}_z\\ -\partial_x\left(\frac{1}{\epsilon_r}\right)e^{i\mathbf{q}\cdot\mathbf{r}}\bar{U}_z-\frac{\pi i q_x}{d_x\epsilon_r}e^{i\mathbf{q}\cdot\mathbf{r}}\bar{U}_z-\frac{1}{\epsilon_r}e^{i\mathbf{q}\cdot\mathbf{r}}\partial_x\bar{U}_z\\ 0\end{bmatrix}, \quad (2.36)$$

and, similarly,

$$\nabla\times\left(\frac{1}{\epsilon_r}\mathbf{D}^*\right)=\begin{bmatrix}\partial_y\left(\frac{1}{\epsilon_r}\right)e^{i\mathbf{q}\cdot\mathbf{r}}\bar{U}_z^*-\frac{\pi i q_y}{d_y\epsilon_r}e^{i\mathbf{q}\cdot\mathbf{r}}\bar{U}_z^*+\frac{1}{\epsilon_r}e^{i\mathbf{q}\cdot\mathbf{r}}\partial_y\bar{U}_z^*\\ -\partial_x\left(\frac{1}{\epsilon_r}\right)e^{i\mathbf{q}\cdot\mathbf{r}}\bar{U}_z^*+\frac{\pi i q_x}{d_x\epsilon_r}e^{i\mathbf{q}\cdot\mathbf{r}}\bar{U}_z^*-\frac{1}{\epsilon_r}e^{i\mathbf{q}\cdot\mathbf{r}}\partial_x\bar{U}_z^*\\ 0\end{bmatrix}. \quad (2.37)$$

When we take the product of Eqs. (2.36) and (2.37), the exponential terms are cancelled, leaving

$$\left[\nabla\times\left(\frac{1}{\epsilon_r}\mathbf{D}^*\right)\right]\cdot\frac{1}{\mu_r}\cdot\left[\nabla\times\left(\frac{1}{\epsilon_r}\mathbf{D}\right)\right]=\bar{U}_z^*\bar{\mathbf{A}}\frac{1}{\mu_r}\bar{\mathbf{B}}\bar{U}_z, \quad (2.38)$$

where

$$\begin{aligned}\bar{\mathbf{A}}&=\begin{pmatrix}[\partial_y(\epsilon_r^{-1})]+\overleftarrow{\partial_y}\frac{1}{\epsilon_r}-\frac{\pi i q_y}{d_y\epsilon_r}\\ -[\partial_x(\epsilon_r^{-1})]-\overleftarrow{\partial_x}\frac{1}{\epsilon_r}+\frac{\pi i q_x}{d_x\epsilon_r}\end{pmatrix}^T,\\ \bar{\mathbf{B}}&=\begin{pmatrix}[\partial_y(\epsilon_r^{-1})]+\frac{1}{\epsilon_r}\overrightarrow{\partial_y}+\frac{\pi i q_y}{d_y\epsilon_r}\\ -[\partial_x(\epsilon_r^{-1})]-\frac{1}{\epsilon_r}\overrightarrow{\partial_x}-\frac{\pi i q_x}{d_x\epsilon_r}\end{pmatrix}.\end{aligned} \quad (2.39)$$

The action integral can then be expressed as

$$\mathcal{A} = \int_{\Omega} d^2r \left[\bar{U}_z^* \bar{\mathbf{A}} \frac{1}{\mu_r} \bar{\mathbf{B}} \bar{U}_z - \frac{1}{\epsilon_r} \bar{U}_z^* \bar{U}_z \right]. \tag{2.40}$$

The action integrals defined in Eqs. (2.31) and (2.40) can be used to calculate the band structures for TE- and TM-modes, respectively.

2.1.4 The Brillouin Zone

As shown in Eq. (2.17), it is only necessary to consider the eigenvalues over a finite range of $\mathbf{q}$. This range of $\mathbf{q}$ values is the first Brillouin zone; outside this zone the eigenvalues will behave periodically. Furthermore, due to reflection symmetries, it is possible to further reduce the Brillouin zone further to obtain a greater density of sampling points for the same computational cost. In the first example considered, a square array of cylindrical dielectric posts, the Brillouin zone only needs to be treated over the region marked in Fig. 2.2.

The band gaps of the photonic crystal may be determined by choosing a large number of ordered pairs (q_x, q_y) from within the irreducible Brillouin zone to determine which eigenvalues will propagate. Then the band structure in the remainder of the Brillouin zone may be determined via reflection symmetry. The entire first Brillouin zone may then be translated to adjacent zones due to the periodicity of the cell function.

In the following, we consider two examples of photonic crystals. The first is a square lattice of dielectric posts, for which we obtain the photonic band structure as previously reported in Joannopoulos. [22] We also identify the symmetries at various points in the dispersion relations to discuss band anti-crossing and level degeneracies at special points. The eigenvector fields at various points of the bands are shown, and frequency bands over the full Brillouin zone are displayed.

The second example is that of a checker-board lattice of dielectric regions. Here again we provide the group theoretic analysis, the band structure,

the band surfaces over the Brillouin zone, and the eigenvector fields.

2.1.5 Group Representation Theory and Photonic Crystals

The eigenvector fields can be organized according to their symmetries with respect to the symmetry group of the crystal and to the group of the wavevector. An excellent exposition on the application of group representation theory to physics is provided by Dresselhaus. [6]

In the following, we follow the group-theoretic analysis of Sakoda. [13–15] The point group of the cylindrical post unit cell is C_{4v}, or the symmetry of the square. The character table of this group is shown in Table 2.1. The wavevector at the Γ-point has the full symmetry of C_{4v}. The symmetry of the Γ-point modes can be deduced by inspecting the transformation properties of the eigenvectors that are transverse to the extrusion direction of the crystal. For a one-dimensional irreducible representation D_i, operation R_j in class j with character $\chi_i(R_j)$, and eigenvector field v, the eigenvector field will transform according to

$$D_i(R_j)\, v = \chi_i(R_j)\, v. \tag{2.41}$$

By inspecting the transformation of v by several $D_i(R_j)$, the character table can be used to deduce which irreducible representation the eigenvector field belongs to. As an example, consider the Γ-point mode in Fig. 2.7(a). The transverse vector field satisfies

$$D_i(C_2)v = v, \quad D_i(2C_4)v = v, \quad D_i(2\sigma_v)v = -v. \tag{2.42}$$

This mode must therefore belong to the irreducible representation with characters

$$\chi_i(C_2) = 1, \quad \chi_i(2C_4) = 1, \quad \chi_i(2\sigma_v) = -1, \tag{2.43}$$

which corresponds to the Γ_2 representation.

For modes with wavevector away from the Γ-point, the symmetry of the wavevector itself must also be taken into account, as explained in Fig. 2.3. The M-point has the full symmetry of C_{4v}. The X-point has the reduced symmetry group C_{2v} (the symmetry of the rectangle) with the character table given in table 2.2. Points along Δ, Z, and Σ have the still further reduced

symmetry of C_{1h} (bilateral symmetry) with the character table given in Table 2.3. Points along Z have C_{1h} symmetry due to the fact that a mirror through the line orthogonal to the q_x direction brings Z to $Z + Q$, where Q is a reciprocal lattice translation vector.

The dispersion relations for the lowest few modes of the cylindrical post labeled by their irreducible representations are shown in Fig.2.5. Notice that in Fig. 2.6 there is an anticrossing site in the TE modes along Z. Since the irreducible representations form an orthogonal basis, anitcrossings can only occur between modes within the same irreducible representation. Indeed, this is the case here, as the two anticrossing modes are in the Z_2 irreducible representation.

Table 2.1: The character table for the group C_{4v}, the symmetry group of the square, is given. For the cylindrical dielectric post structure, this symmetry is exhibited at the Γ- and M-points in the Brillouin zone.

C_{4v}			E	C_2	$2C_4$	$2\sigma_v$	$2\sigma_d$
x^2+y^2, z^2	z	Γ_1	1	1	1	1	1
	R_z	Γ_2	1	1	1	-1	-1
x^2-y^2		Γ_1'	1	1	-1	1	-1
xy		Γ_2'	1	1	-1	-1	1
(xz, yz)	$(x, y), (R_x, R_y)$	Γ_{12}'	2	-2	0	0	0

Table 2.2: The character table for the group C_{2v}, the symmetry group of the rectangle, is shown. For the cylindrical dielectric post structure, this symmetry is exhibited at the X point of the Brillouin zone.

C_{2v}			E	C_2	σ_v	σ_v'
x^2, y^2, z^2	z	X_1	1	1	1	1
xy	R_z	X_2	1	1	-1	-1
xz	R_y, x	X_1'	1	-1	1	-1
yz	R_x, y	X_2'	1	-1	-1	1

Table 2.3: The character table for the group C_{1h}, which is the bilateral symmetry group, is given. For the cylindrical dielectric post structure, this group is exhibited along the Δ and Σ lines of symmetry in the Brillouin zone.

C_{1h}			E	σ_v
x^2, y^2, z^2, xy	R_z, x, y	Δ_1	1	1
xz, yz	R_x, R_y, z	Δ_2	1	-1

2.2 Eigenstates for periodic dielectric posts

The band structure for the lattice of dielectric posts was computed using a mesh of 4420 nodes, yielding a matrix size of 26520×26520. The mesh was refined in the region surrounding the edge of the cylindrical post. The curves shown in Fig. 2.5 give the behavior of the propagating frequencies of radiation at various points along the edge of the irreducible part of the Brillouin zone. The finite element method reproduces a band gap in the TM modes which is also predicted by the planewave method. Using finite elements, it is also possible to increase the resolution close to the anticrossing site marked in Fig. 2.5. This is a location at which multiple eigenvalues of the same polarization (i.e. both TM or both TE) appear to touch. The close-up view of this point on the edge of the Brillouin zone is given in Fig. 2.6.

The eigenfunctions for the arrangement of cylindrical dielectric posts are shown in Figs. 2.7-2.9. Note that the point symmetries of each mode at the high symmetry points of Γ, X and M can be used, along with Fig. 2.3 and Tables 2.1-2.3, to verify the symmetry groups shown in Fig. 2.5 by direct observation of the eigenvector fields.

The dispersion relations are calculated for the irreducible Brillouin zone, which is only one eighth of the full Brillouin zone as shown in Fig. 2.2, and then their full reconstruction over the entire zone is performed. This can reduce computation time by a factor of 8. The lowest few TE and TM dispersion relations are shown in Figs. 2.10-2.11. These three-dimensional dispersion surfaces also provide another means of visualizing band gaps in the TE and TM modes, which are of great interest in photonic crystal applications.

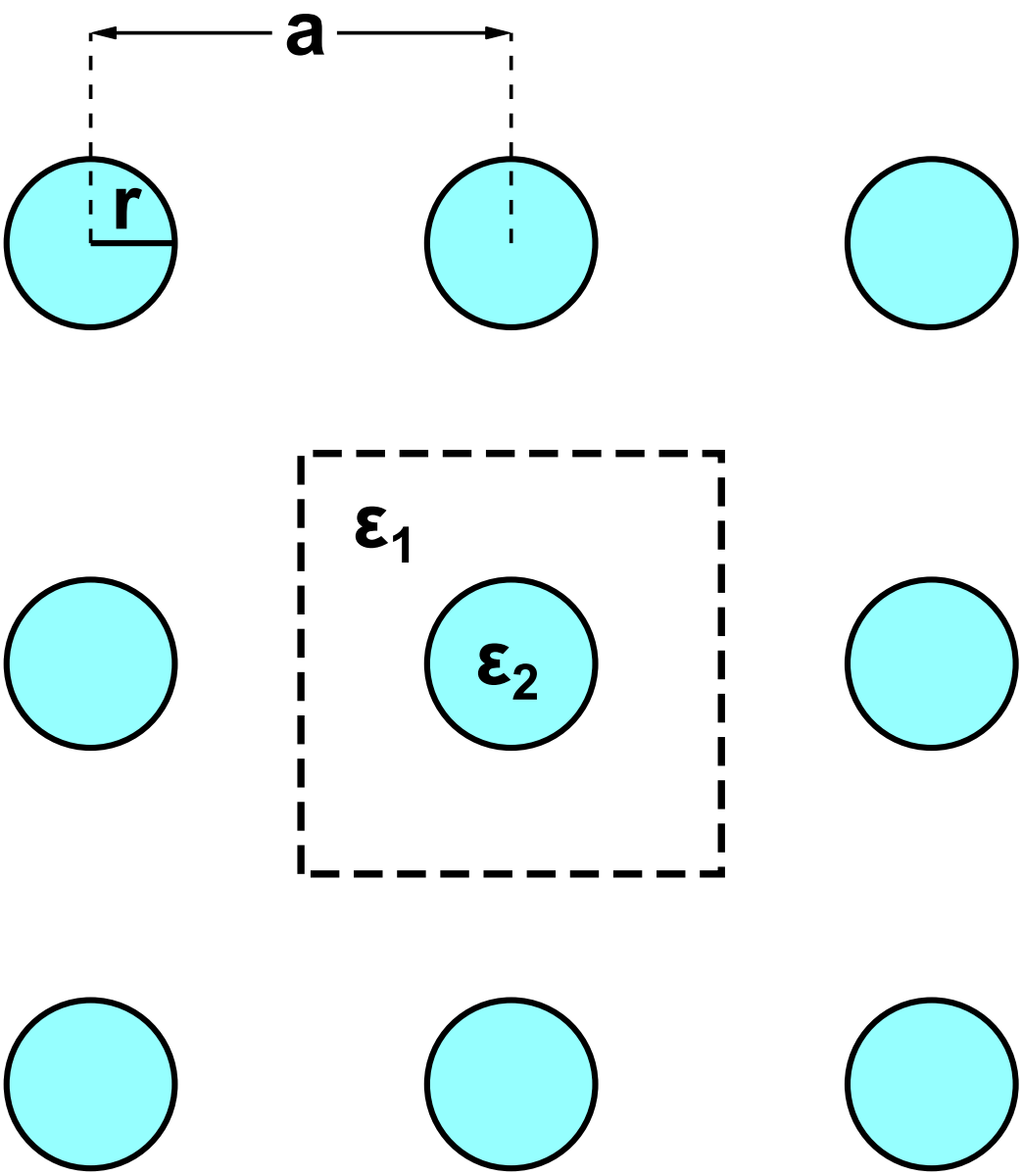

Figure 2.1: An array of cylindrical dielectric posts of dielectric constant ϵ_2 arranged periodically in a medium with a dielectric constant ϵ_1 is shown.

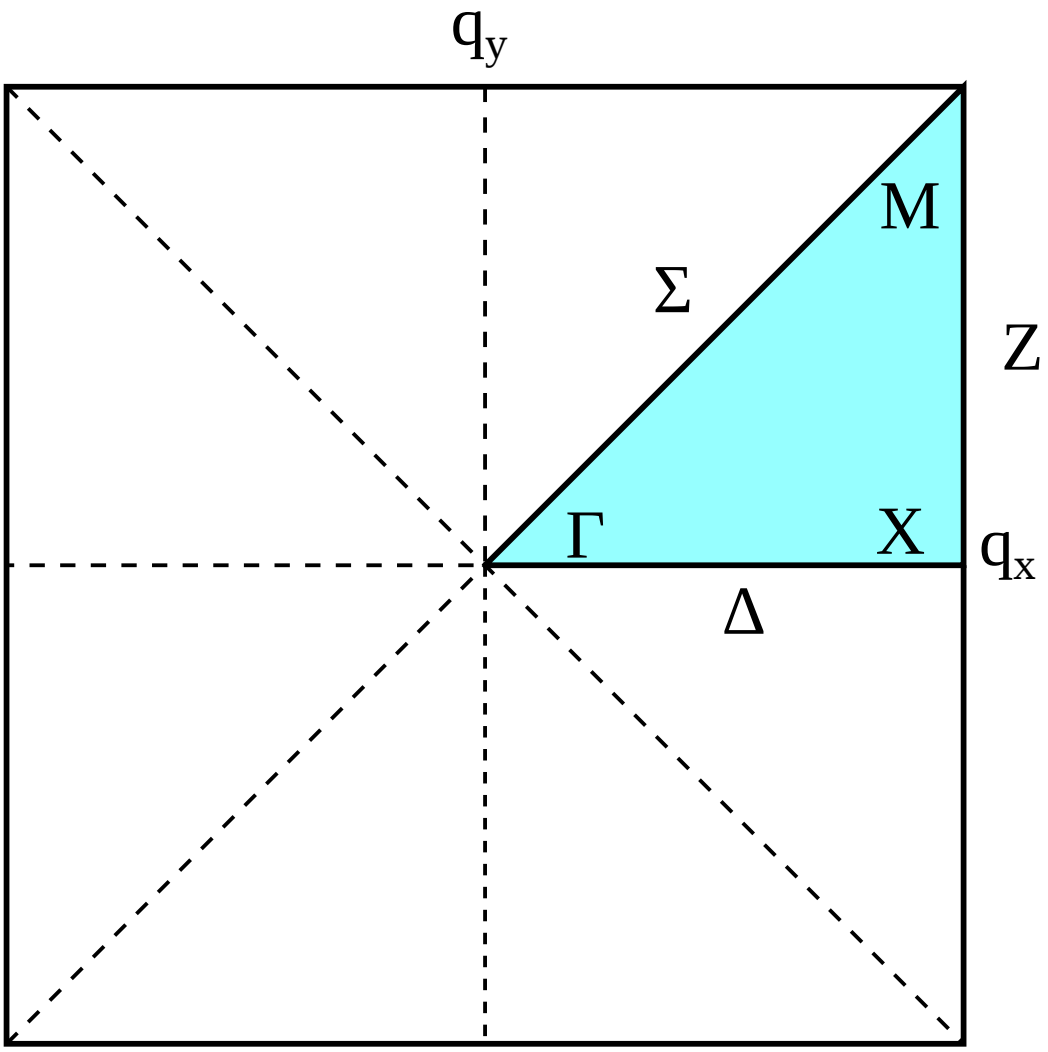

Figure 2.2: The Brillouin zone for a two-dimensional photonic crystal is shown. The maximum and minimum values of the components of **q** are given by Eq. (2.9). The irreducible component of the Brillouin zone has been highlighted. The dashed lines are symmetry lines within the first Brillouin zone.

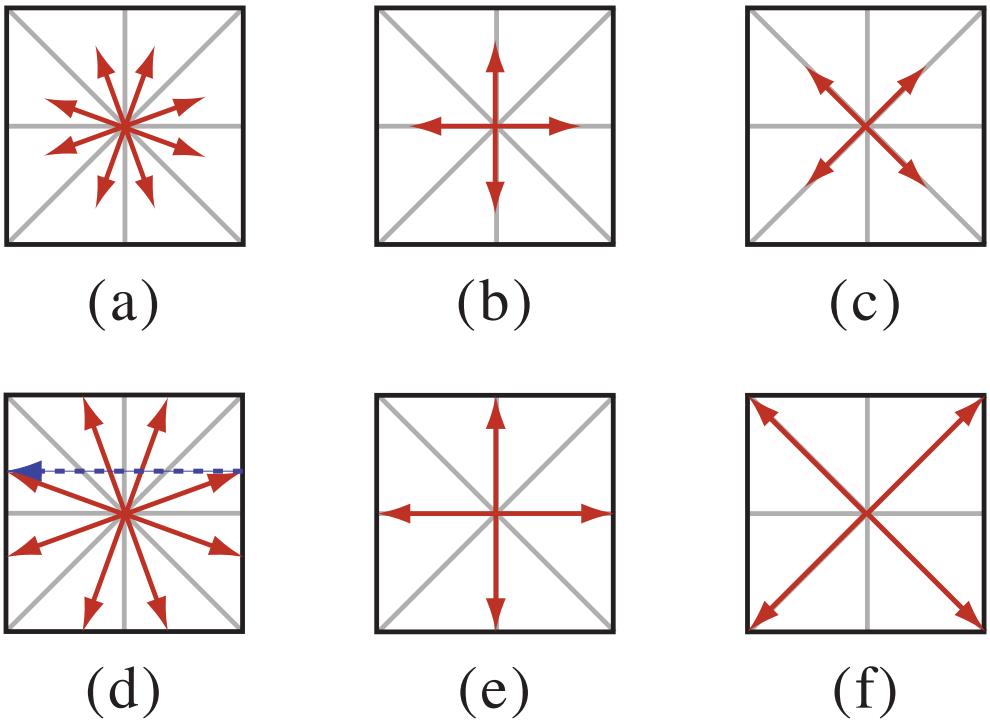

Figure 2.3: Cases when the wavevector is within the Brillouin zone and has (a) only the trivial symmetry of the crystal, (b,c) the symmetry of a subgroup of the crystal, as compared to when the wavevector is on the zone edge (d–f) where some wavevectors are equivalent modulo a reciprocal lattice translation vector, shown as a dashed arrow in (d). The crystal is assumed to have the point group symmetry of the square.

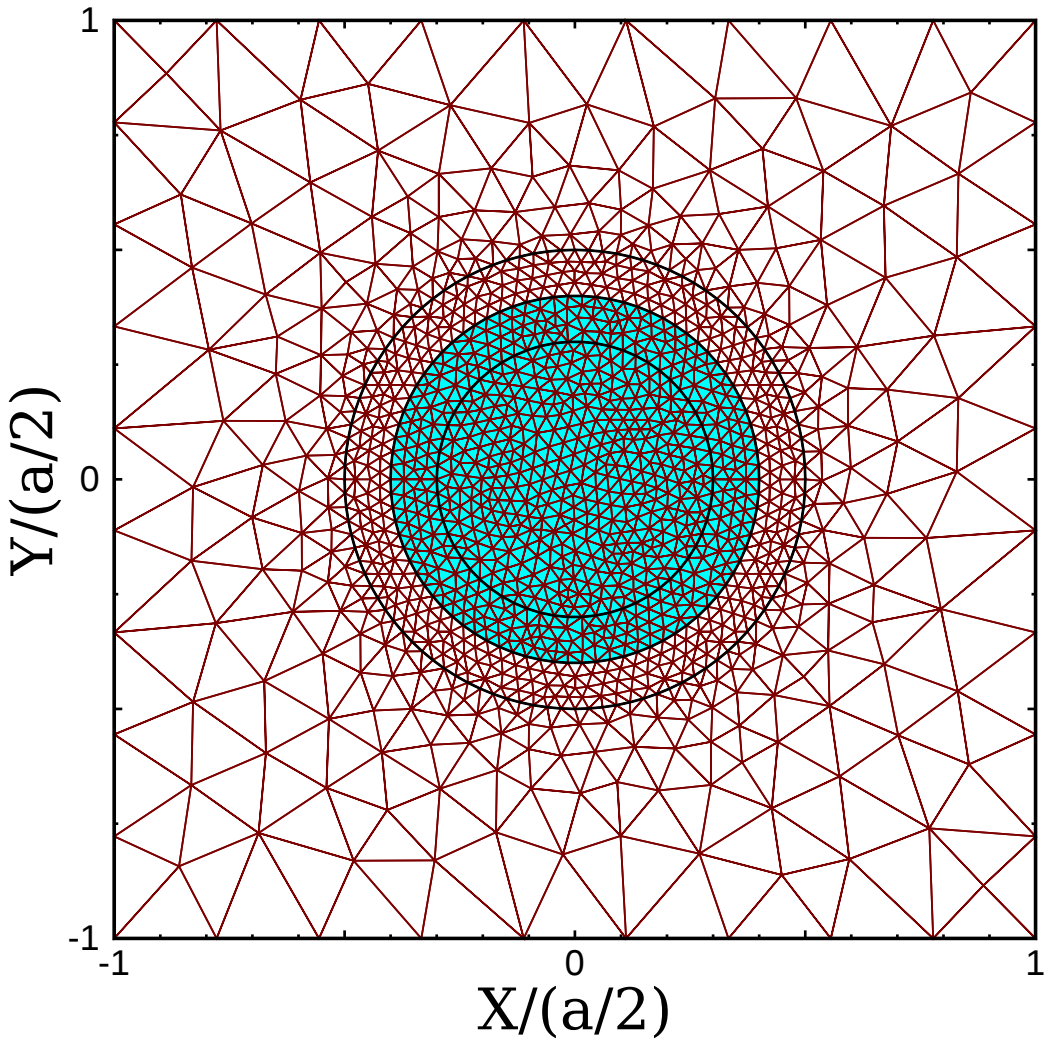

Figure 2.4: A sample mesh is given for the unit cell of a lattice of cylindrical dielectric posts. Significant mesh refinement occurs close to the boundary of the post, where the dielectric changes.

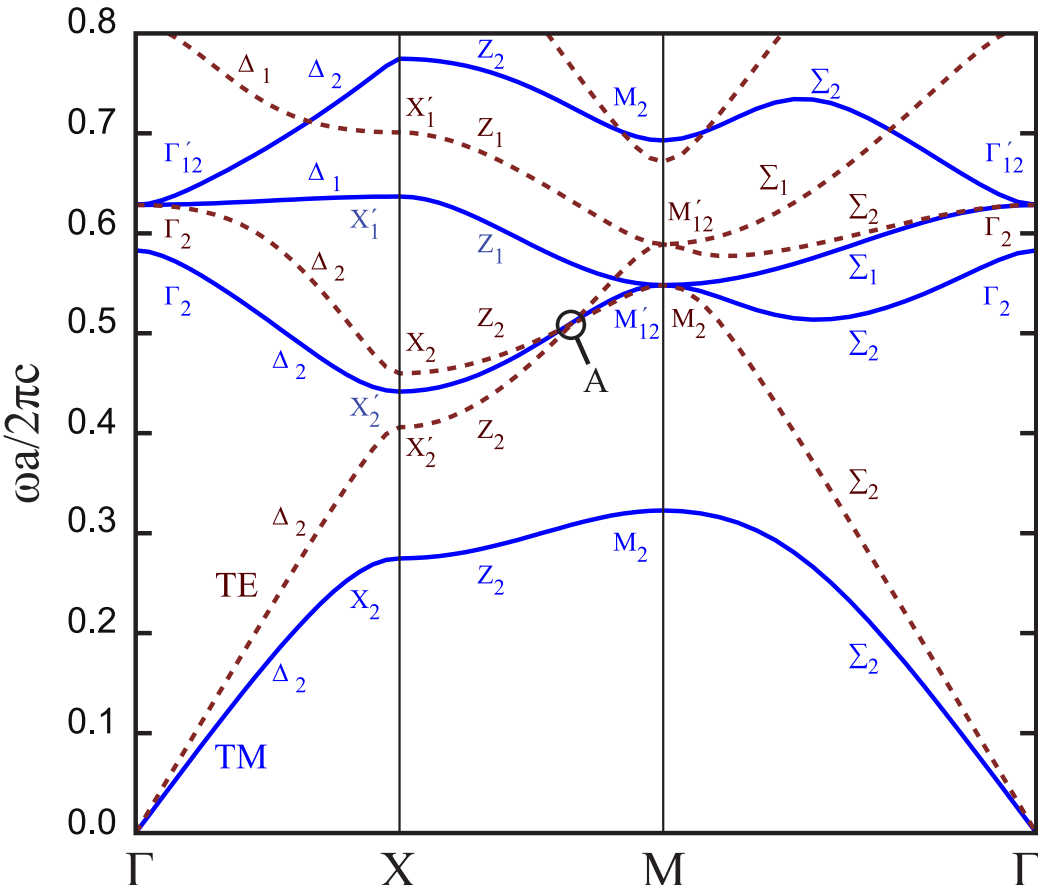

Figure 2.5: Eigenvalues for the transverse electric and transverse magnetic modes as calculated using the finite element method with quintic Hermite interpolation polynomials. The point labeled as A is the location of an anti-crossing site between the lowest and second-lowest TE modes. This location is shown in higher resolution in Fig. 2.6.

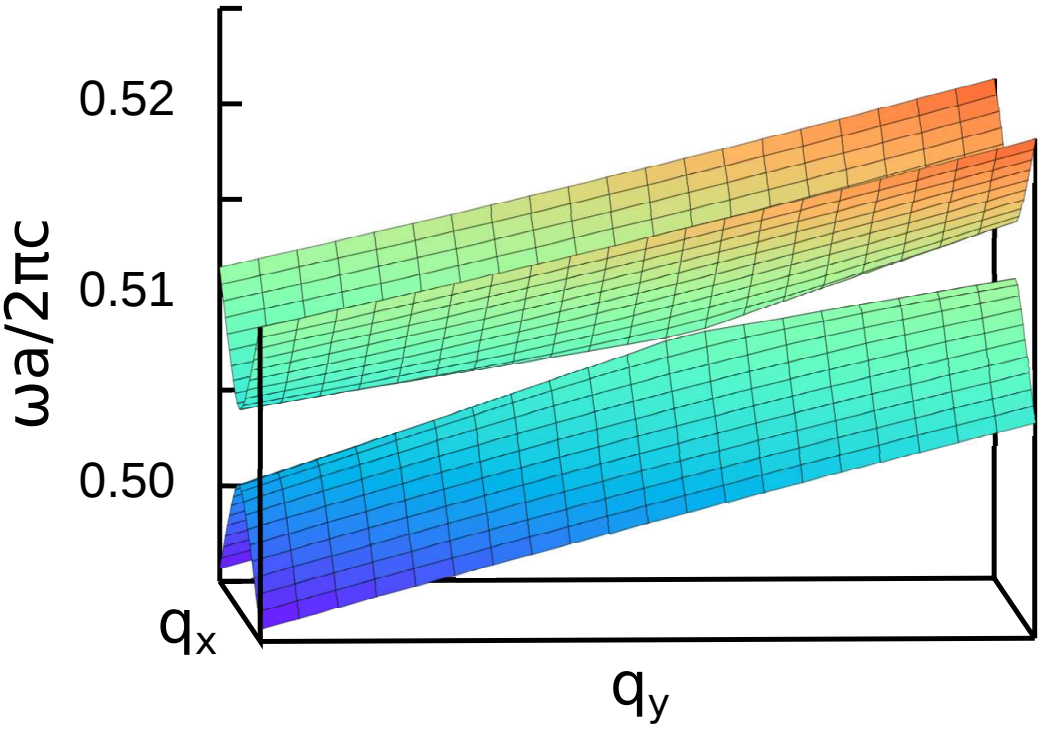

Figure 2.6: Close-up view of the anticrossing site shown at point A in Fig. 2.5.

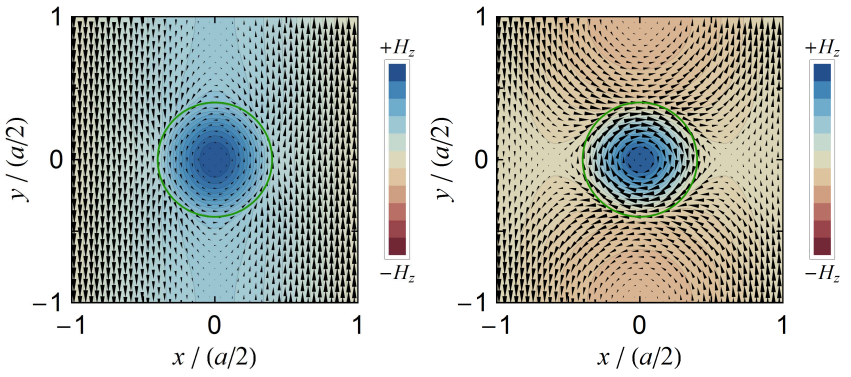

(a) TE mode 2

(b) TE mode 3

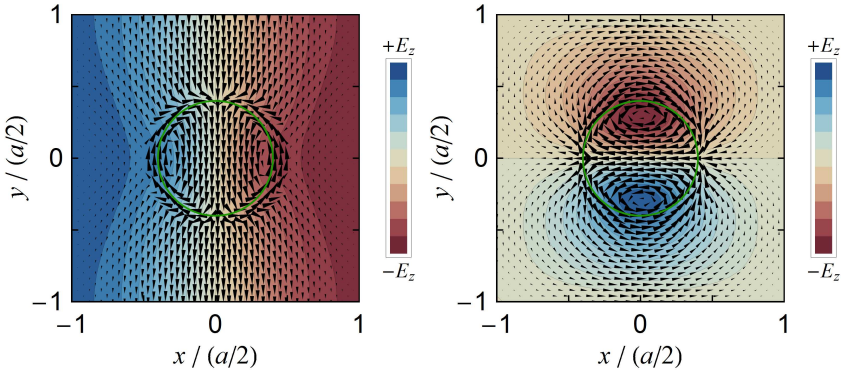

(c) TM mode 2

(d) TM mode 3

Figure 2.7: The electric and magnetic fields of the second and third modes corresponding to the Γ-point in the lattice of cylindrical posts are shown. For TE-modes, the in-plane electric field is represented by vectors and the out-of-plane magnetic field is represented by the gradient background. For TM-modes, the vectors represent the in-plane magnetic field and the background represents the strength of the out-of-plane electric field. Note that the first mode is not shown because the corresponding eigenvalue is zero, resulting in a trivial solution.

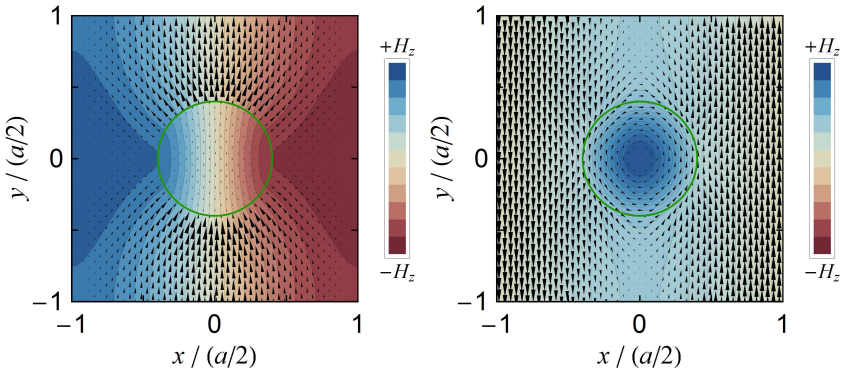

(a) TE mode 1

(b) TE mode 2

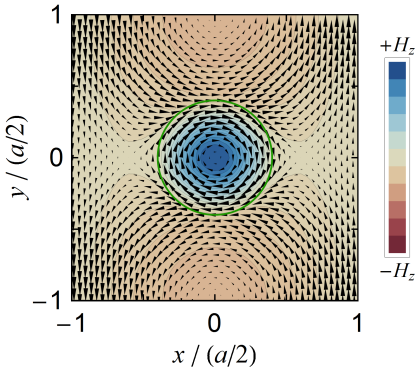

(c) TE mode 3

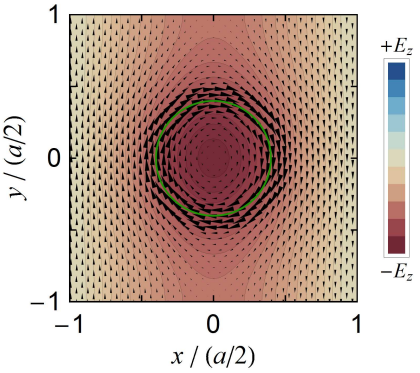

(d) TM mode 1

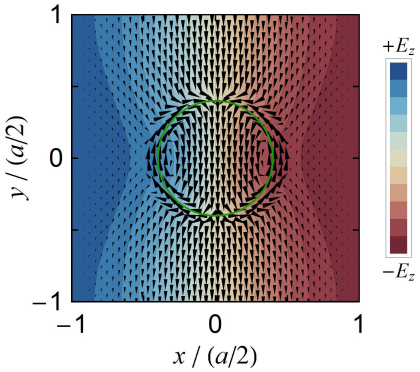

(e) TM mode 2

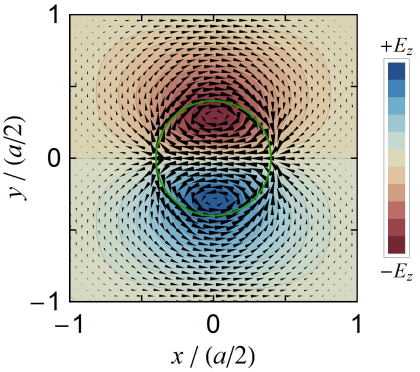

(f) TM mode 3

Figure 2.8: The electric and magnetic fields of the first three modes corresponding to the X-point in the lattice of cylindrical posts are shown. For TE-modes, the in-plane electric field is represented by vectors and the out-of-plane magnetic field is represented by the gradient background. For TM-modes, the vectors represent the in-plane magnetic field and the background represents the strength of the out-of-plane electric field.

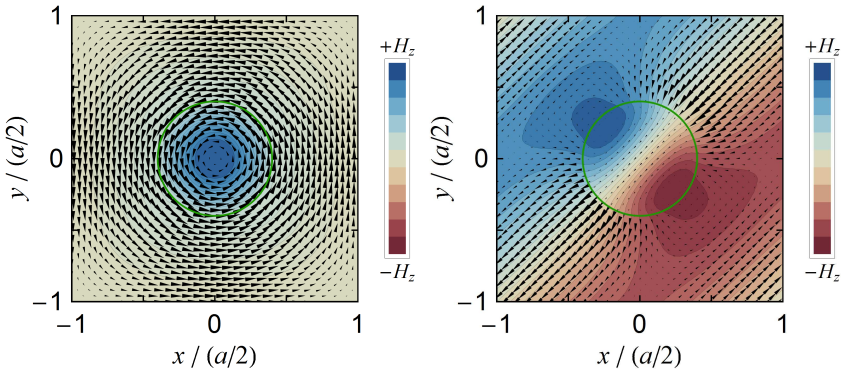

(a) TE mode 1

(b) TE mode 2

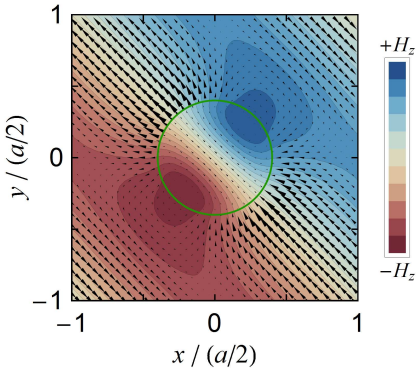

(c) TE mode 3

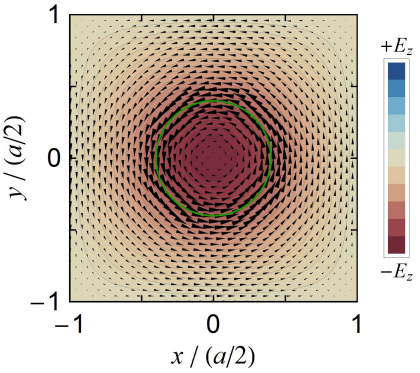

(d) TM mode 1

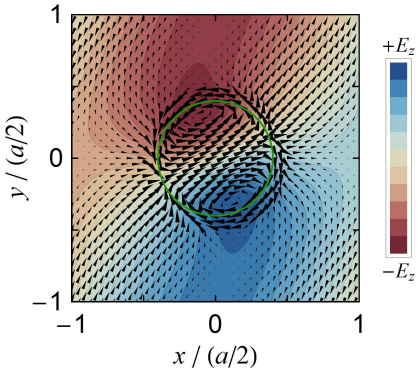

(e) TM mode 2

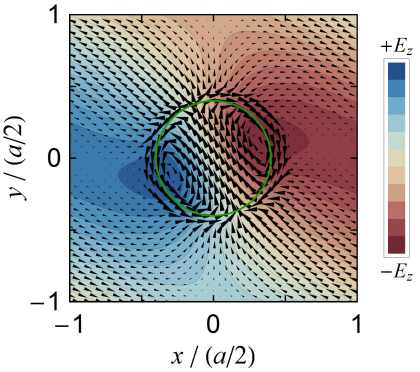

(f) TM mode 3

Figure 2.9: The electric and magnetic fields of the first three modes corresponding to the M-point in the lattice of cylindrical posts are shown. For TE-modes, the in-plane electric field is represented by vectors and the out-of-plane magnetic field is represented by the gradient background. For TM-modes, the vectors represent the in-plane magnetic field and the background represents the strength of the out-of-plane electric field.

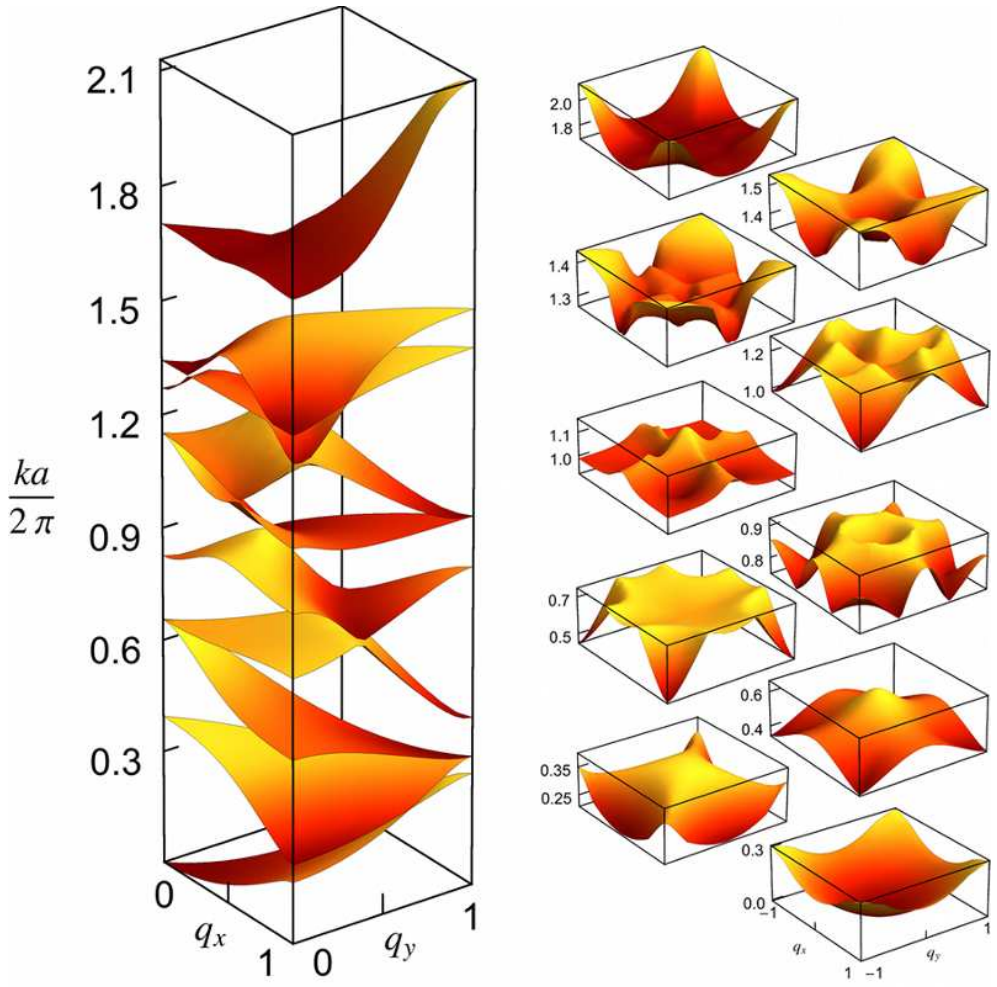

Figure 2.10: The eigenvalues of the transverse electric modes of the periodic lattice of dielectric posts are plotted as surfaces in the first Brillouin zone. On the left, the first ten eigenvalues are shown in the irreducible part of the Brillouin zone. On the right, each eigenvalue has been separated from the rest and extended to the full Brillouin zone through symmetry operations.

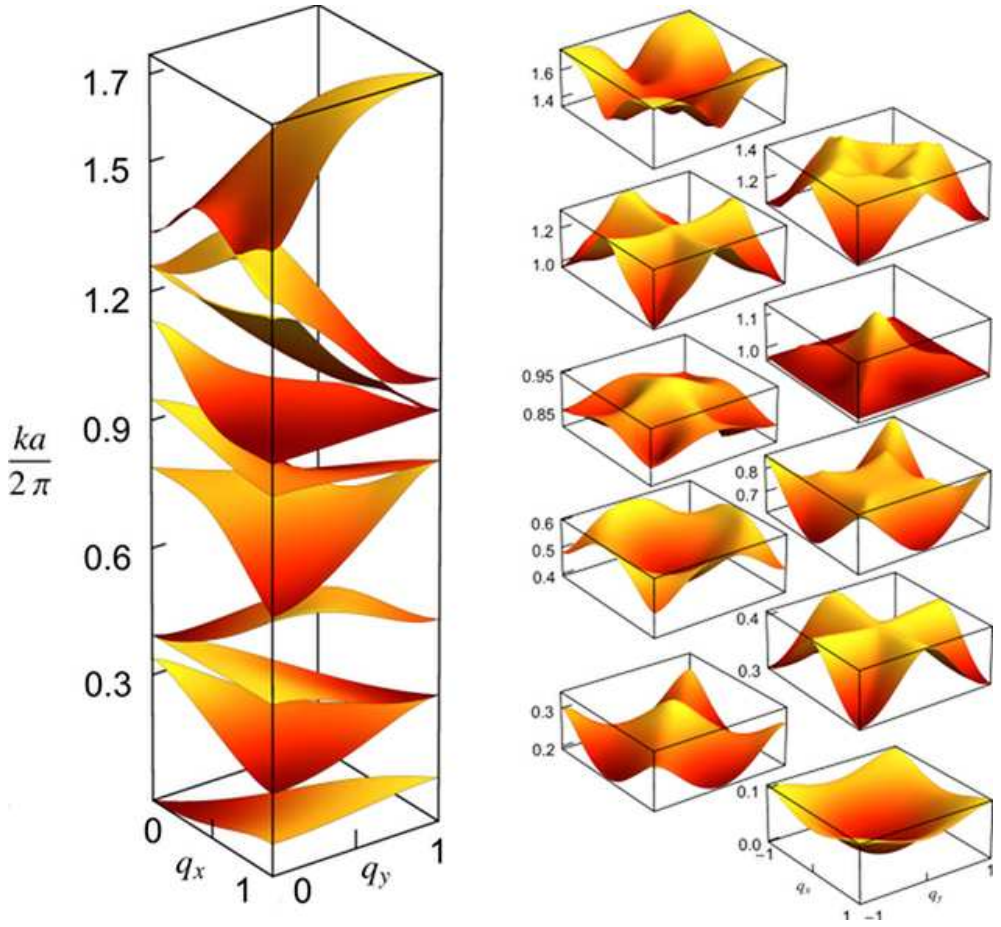

Figure 2.11: The eigenvalues of the transverse magnetic modes of the periodic lattice of dielectric posts are plotted as surfaces in the first Brillouin zone. On the left, the first ten eigenvalues are shown in the irreducible part of the Brillouin zone. On the right, each eigenvalue has been separated from the rest and extended to the full Brillouin zone through symmetry operations. When the eigenvalues are plotted together, a band gap can be seen between the first and second eigenvalue surfaces, as shown on the left.

2.3 Eigenstates for a checkerboard lattice

The band structure for a checkerboard lattice was computed using a mesh of 12355 nodes, yielding a matrix size of 74130×74130. The mesh was refined in the region surrounding the edges within the checkerboard. Since the checkerboard lattice has more internal boundaries per unit cell than the cylindrical post geometry, a greater degree of mesh refinement was required, resulting in a larger global matrix than that of the lattice of cylindrical posts.

The eigenvalues are plotted over a triangular path between the Γ, X and S points. Compared to the dielectric posts, the checkerboard shows much more activity and a denser band structure at low frequencies, but it has a smaller band gap in the TM modes. Like the cylindrical posts, this checkerboard has no TE band gap. The corresponding eigenfunctions for the lowest modes at the high-symmetry points are plotted in Figs. 2.15(a)-2.18(f).

The vectors represent the electric field in TE modes and the magnetic field in TM modes, while the shading of the background represents the intensity of the magnetic field in TE modes and the electric field in TM modes, with lighter shades corresponding to regions of greater field magnitude. Note that the eigenfunction for the lowest eigenvalue is omitted for the Γ-point for both modes of propagation. This is because those lowest eigenvalues approach zero at the Γ-point, causing the corresponding eigenfunctions to be trivial (zero everywhere).

The dispersion relations calculated for the irreducible Brillouin zone and then their full reconstruction over the entire zone is performed. The lowest few TE and TM dispersions are shown in Figs. 2.19-2.20.

In conclusion, we anticipate that the use of Hermite FEM will allow the treatment of multiscale problems associated with photonic crystals with embedded quantum dots, defects, and the like. The spatial representation of the fields using Hermite triangular interpolation is much more economical than employing plane-wave methods for such structures allowing the deployment of more finite elements strategically in specific regions as needed. The resulting global matrices are still sparse and banded due to the local connectivity, which leads to far more compact matrices than in other schemes with the concomitant reduction in compute-time.

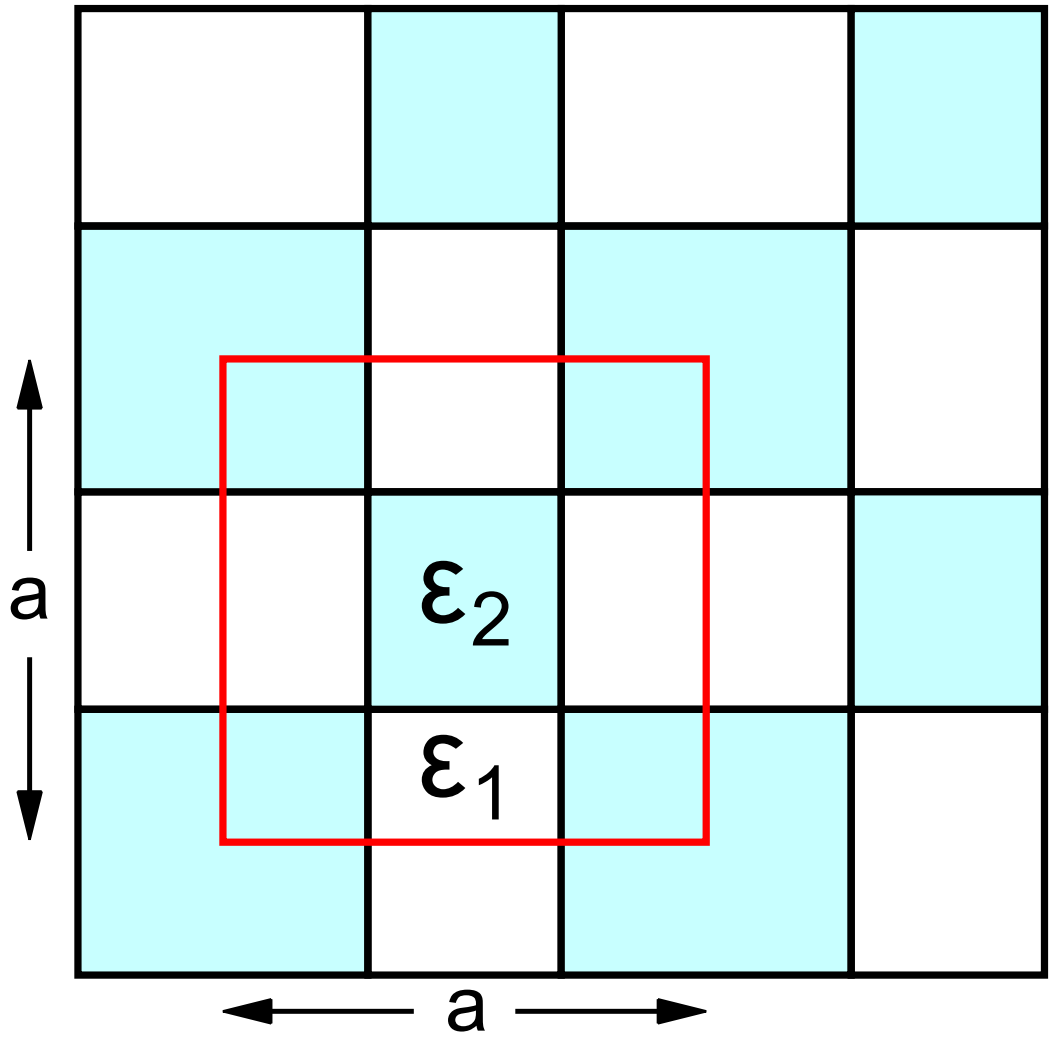

Figure 2.12: A periodic checkerboard pattern with two alternating dielectric materials is shown. Note that the sizes of adjacent checkers within a single unit cell do not necessarily match.

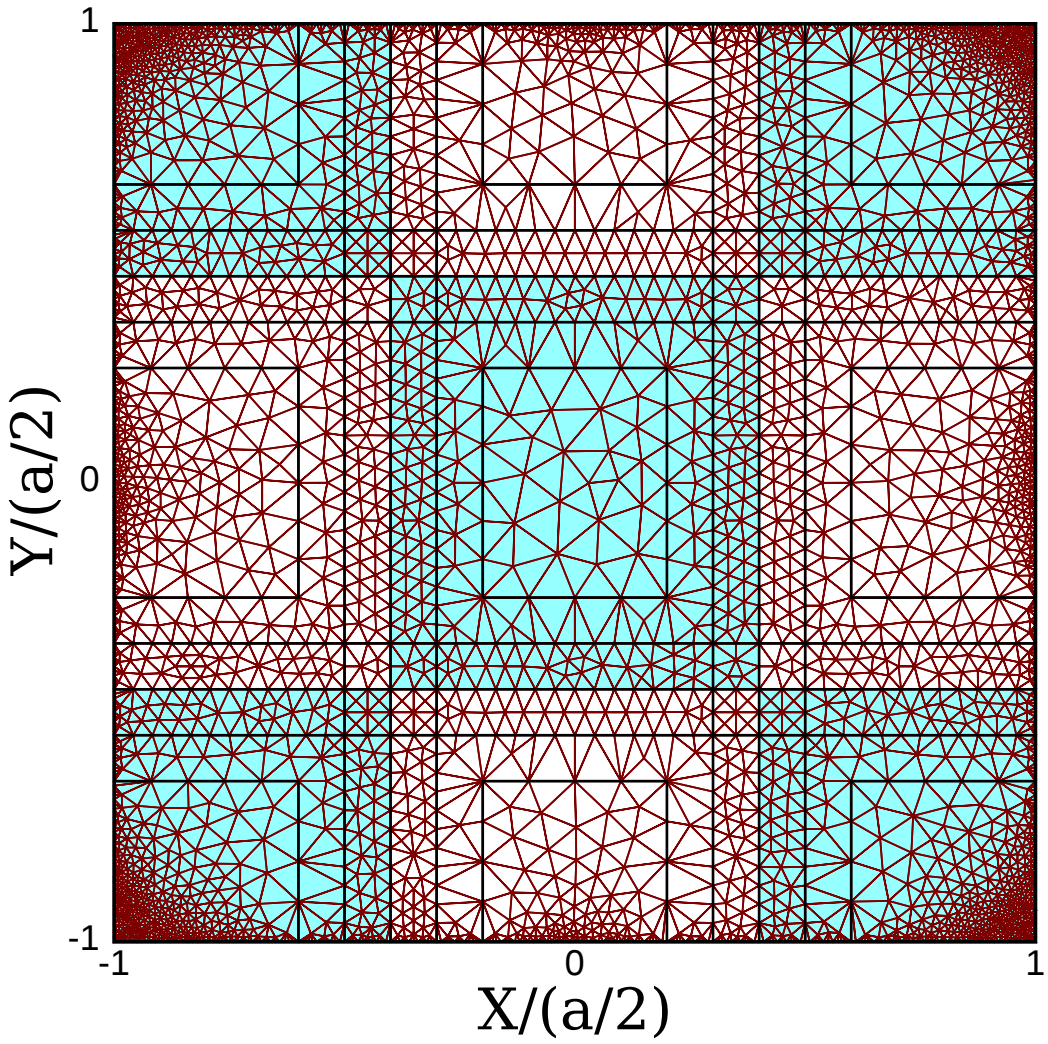

Figure 2.13: A sample finite element mesh is given for the unit cell of a checkerboard lattice. Mesh refinement occurs at all of the checker boundaries.

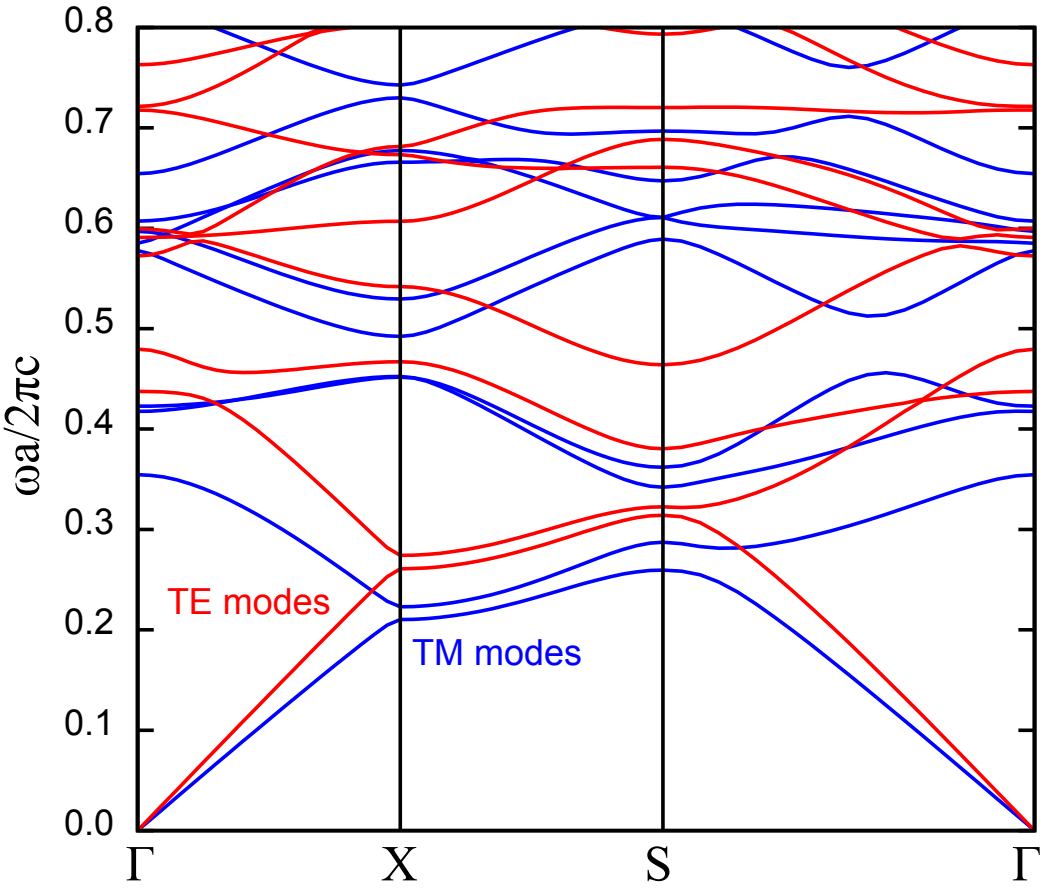

Figure 2.14: Eigenvalues for the transverse electric and transverse magnetic modes for the checkerboard arrangement.

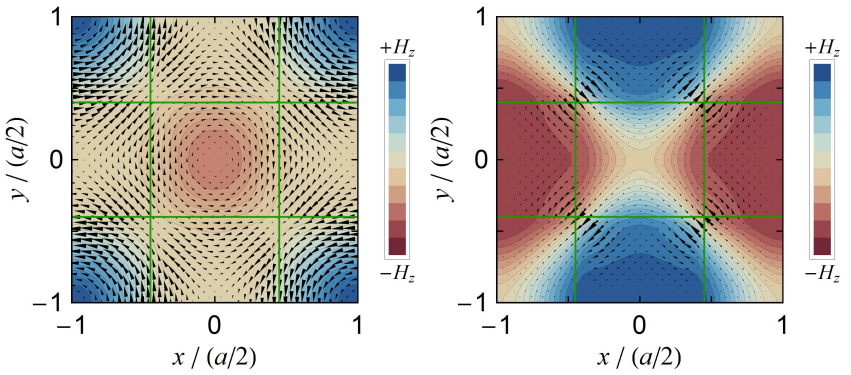

(a) TE mode 2

(b) TE mode 3

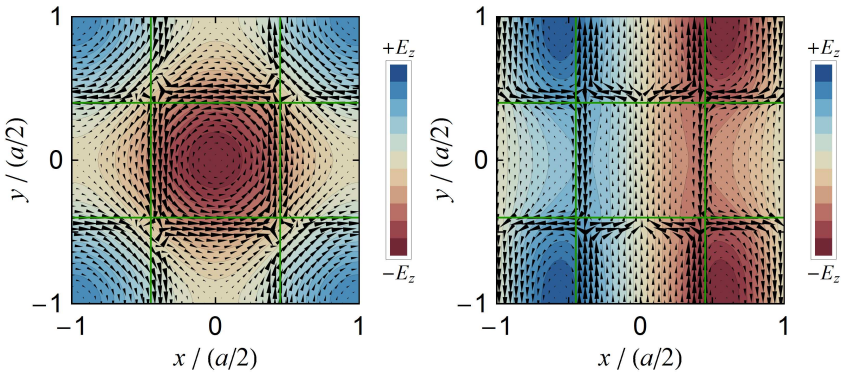

(c) TM mode 2

(d) TM mode 3

Figure 2.15: The electric and magnetic fields of the second and third modes corresponding to the Γ-point in the checkerboard lattice are shown. For TE-modes, the in-plane electric field is represented by vectors and the out-of-plane magnetic field is represented by the gradient background. For TM-modes, the vectors represent the in-plane magnetic field and the background represents the strength of the out-of-plane electric field. Note that the first mode is not shown because the corresponding eigenvalue is zero, resulting in a trivial solution.

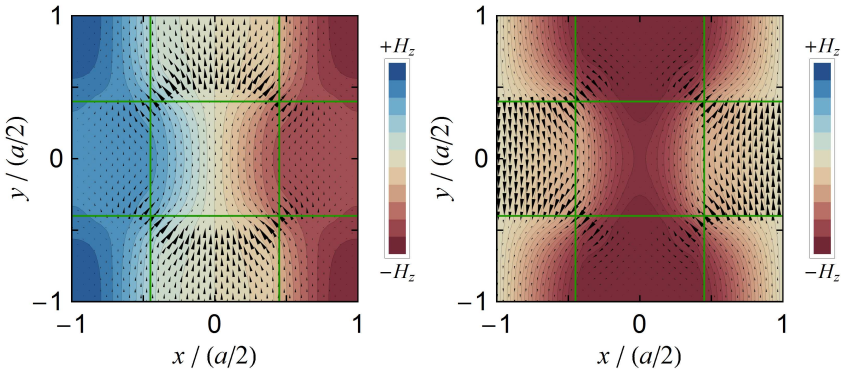

(a) TE mode 1

(b) TE mode 2

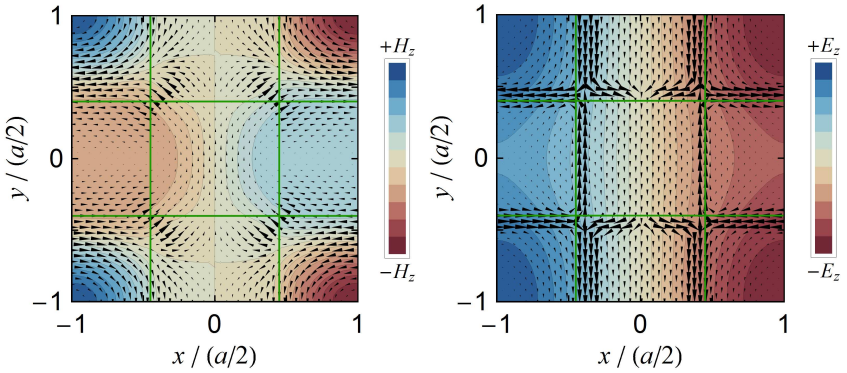

(c) TE mode 3

(d) TM mode 1

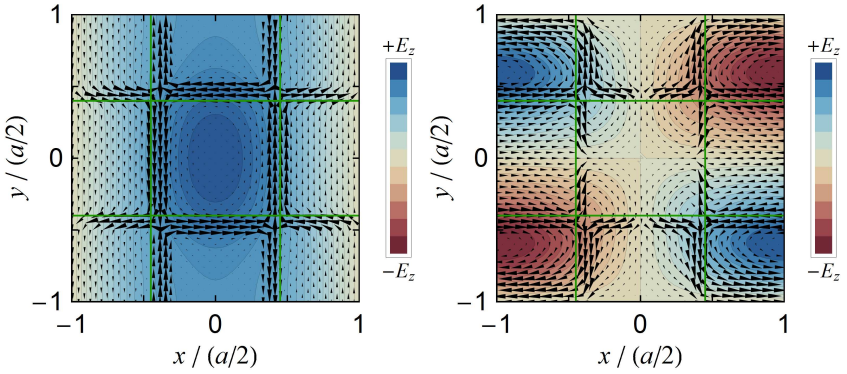

(e) TM mode 2

(f) TM mode 3

Figure 2.16: The electric and magnetic fields of the first three modes corresponding to the X-point in the checkerboard lattice are shown. For TE-modes, the in-plane electric field is represented by vectors and the out-of-plane magnetic field is represented by the gradient background. For TM-modes, the vectors represent the in-plane magnetic field and the background represents the strength of the out-of-plane electric field.

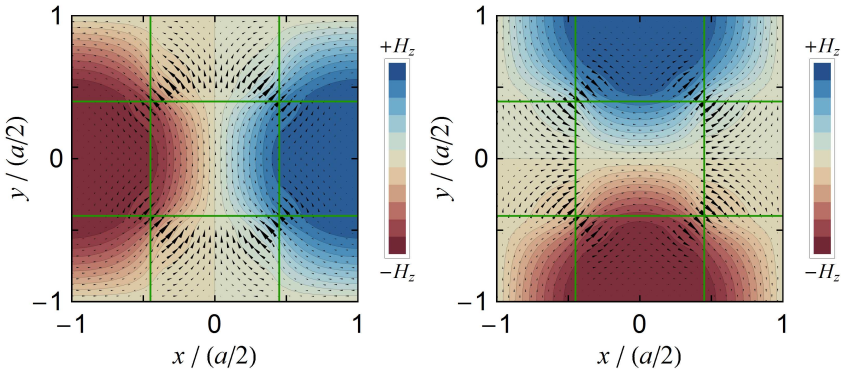

(a) TE mode 1

(b) TE mode 2

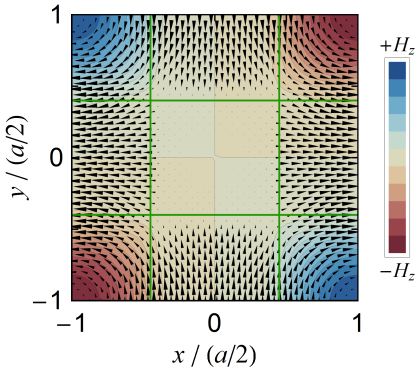

(c) TE mode 3

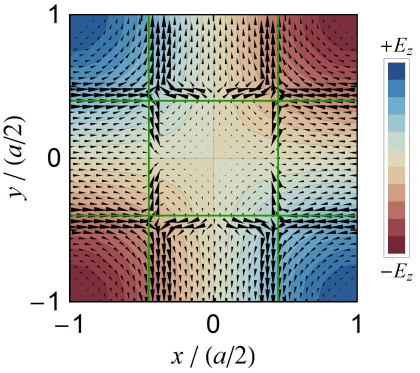

(d) TM mode 1

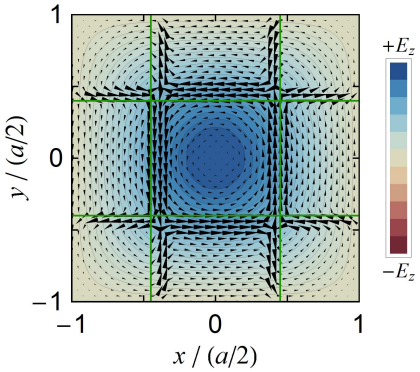

(e) TM mode 2

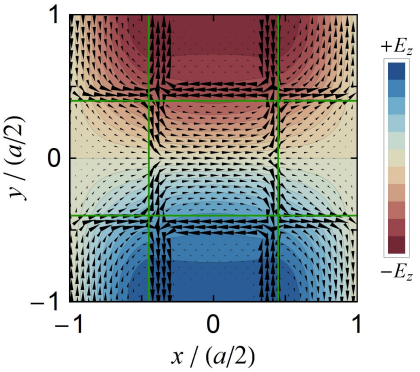

(f) TM mode 3

Figure 2.17: The electric and magnetic fields of the first three modes corresponding to the S-point in the checkerboard lattice are shown. For TE-modes, the in-plane electric field is represented by vectors and the out-of-plane magnetic field is represented by the gradient background. For TM-modes, the vectors represent the in-plane magnetic field and the background represents the strength of the out-of-plane electric field.

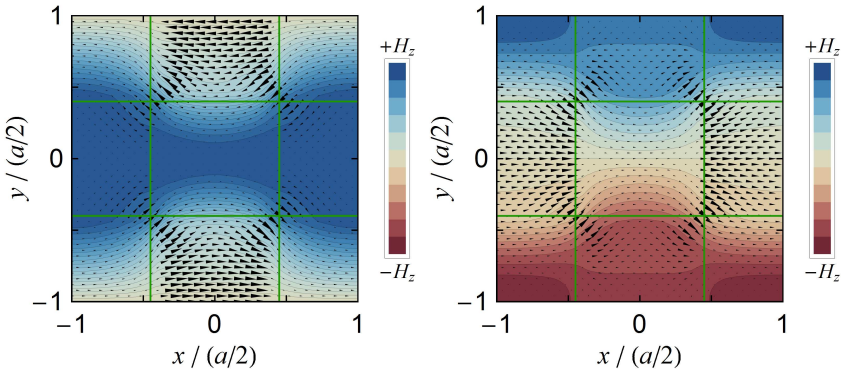

(a) TE mode 1

(b) TE mode 2

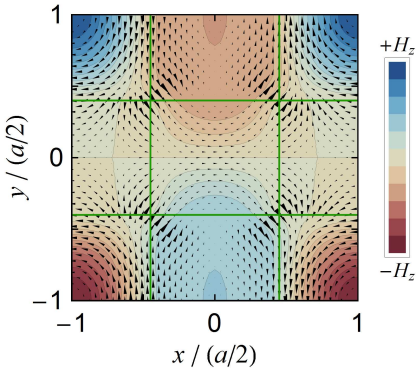

(c) TE mode 3

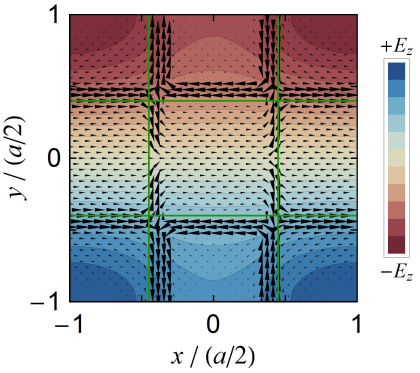

(d) TM mode 1

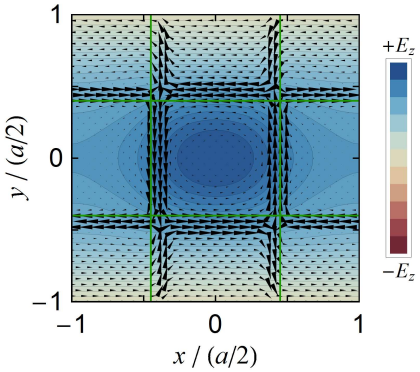

(e) TM mode 2

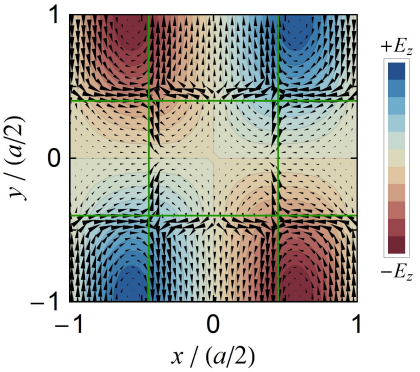

(f) TM mode 3

Figure 2.18: The electric and magnetic fields of the first three modes corresponding to the Y-point in the checkerboard lattice are shown. For TE-modes, the in-plane electric field is represented by vectors and the out-of-plane magnetic field is represented by the gradient background. For TM-modes, the vectors represent the in-plane magnetic field and the background represents the strength of the out-of-plane electric field.

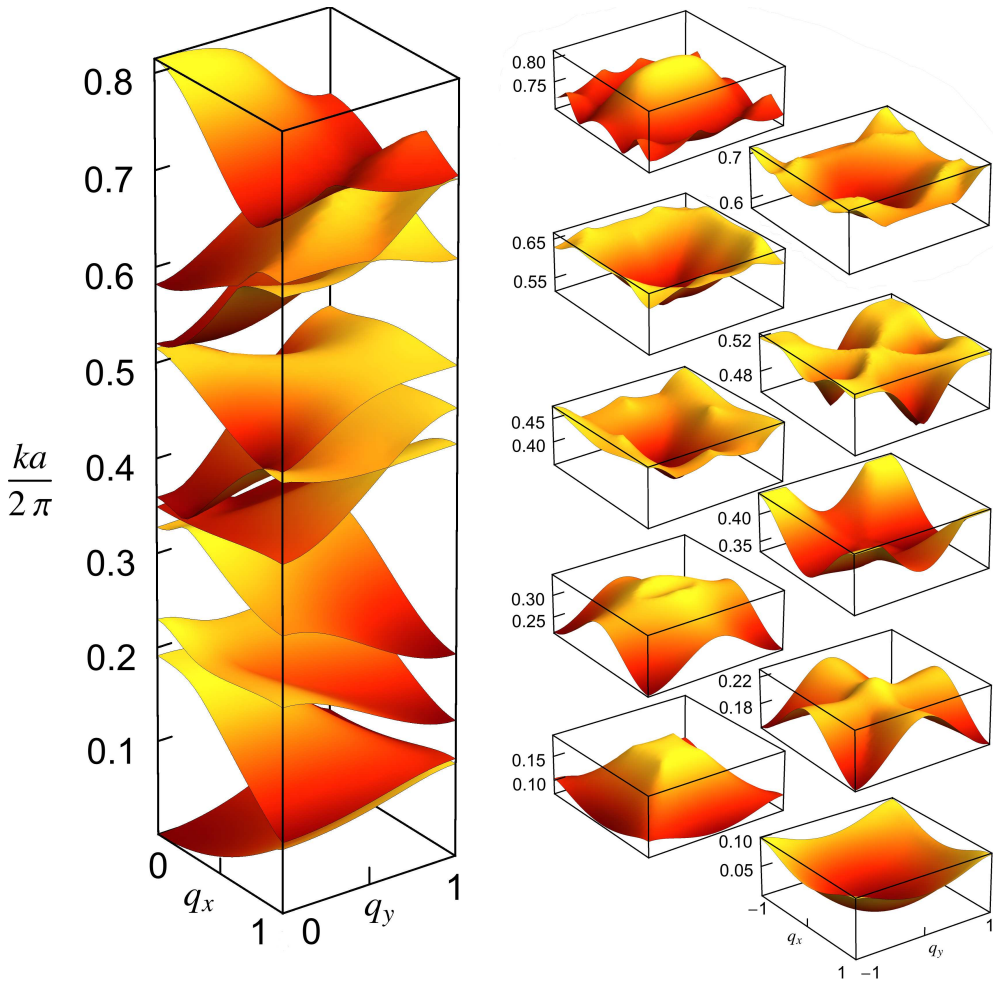

Figure 2.19: The eigenvalues of the transverse electric modes of the checkerboard lattice are plotted as surfaces in the first Brillouin zone. On the left, the first ten eigenvalues are shown in the irreducible part of the Brillouin zone. On the right, each eigenvalue has been separated from the rest and extended to the full Brillouin zone through symmetry operations.

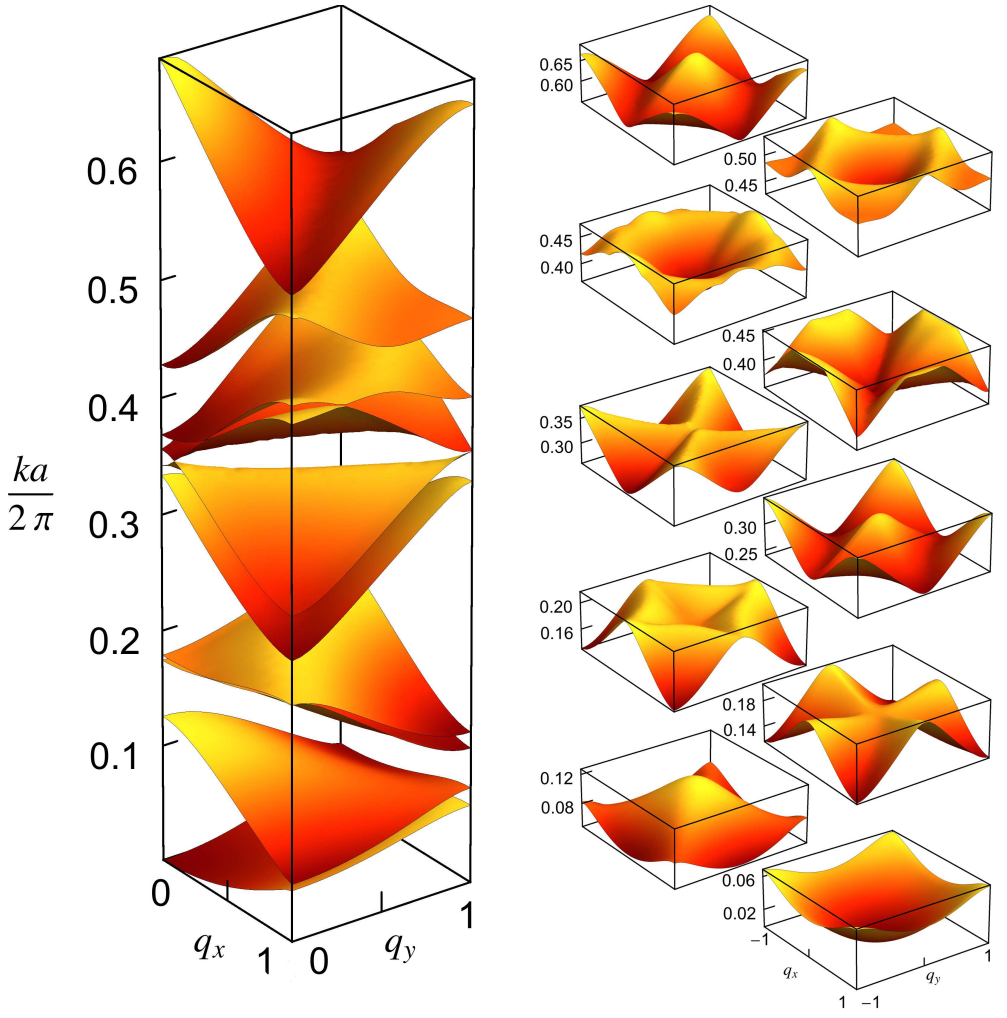

Figure 2.20: The eigenvalues of the transverse magnetic modes of the checkerboard lattice are plotted as surfaces in the first Brillouin zone. On the left, the first ten eigenvalues are shown in the irreducible part of the Brillouin zone. On the right, each eigenvalue has been separated from the rest and extended to the full Brillouin zone through symmetry operations. The only observable band gap for this geometry is a small gap between the fourth and fifth TM modes.

Chapter 3

Concluding remarks

Despite a decades-long history of being overshadowed by plane wave expansion methods, the finite element method offers a flexible, robust means of computing the eigenstates of a photonic crystal. In our calculations, we note that the typical matrix dimensions for the photonic crystal with square geometry containing cylindrical posts are on the order of 26×10^3; however, the local connectivity leads to a banded matrix with 0.158% occupancy. For the checker-board lattice, the discontinuities in the dielectric function required matrices of dimensions 74×10^3, with just 0.056% occupancy. This sparsity is clearly a genuine advantage over the plane-wave method. The ability to construct the field distributions from the nodal eigenvectors with no discontinuities in the reconstructed function and its derivative is an additional benefit. Furthermore, the plane-waves are global functions, and the eigenfunctions constructed using these functions have the usual errors on the order of the square root of the errors in the eigenvalues. However, in the finite element method, this error can be distributed nonuniformly by emphasizing areas (or volumes) of interest through the redistribution of elements, putting more elements in those areas that are of particular interest. This remarkable flexibility is yet another advantage in using FEM. The detailed agreement with the published results for the square lattice of dielectric posts shows that the FEM provides accurate, reliable results that are derivable with banded, sparse matrices. We have included the group-theoretic analysis of the band structure, showing the degeneracies associated with the special points in the Brillouin zone. The anti-crossing of the first and second TE dispersions between the X and M points has been highlighted, and the degeneracies at the special points have been indicated in the displayed wavefunctions. The

reconstructed energy band surfaces over the full Brillouin zone have been presented here for the first time.

We have also included results on the photonic band structure for the checkerboard superlattice of dielectrics. Again, the ease with which the band structure and the wavefunctions are obtained within an FEM framework shows that FEM with Hermite finite elements holds great promise as the method of choice for such calculations.

The finite element approach can tackle multiscale problems such as defects in photonic crystals, quantum dots embedded in waveguides or in photonic crystals, and so on. The plane-wave and spectral methods would be prohibitively expensive computationally to provide high accuracy simulations of such structures.

It is by now evident that the finite element method helps "unlock the magic of Maxwell's equations," to quote Cendes. [23] The remarkable aspects of composite media in which both (or either) the permittivity and the permeability are negative can also be explored within our methodology. [24–26]

If the finite element method is to supplant the plane wave expansion method as the future of photonic crystal modeling, it will be necessary to demonstrate its applicability in three dimensions. The development of a practical, $\mathcal{C}_1$-continuous set of Hermite interpolating polynomials in three dimensions will make this method a feasible option for engineering applications. Indeed, we have already begun such efforts by using group representation theory to establish a routine procedure for the derivation of Hermite interpolation polynomials for arbitrary dimensionality and derivative order of continuity. [5] A final feature that would be required in this context is the exploration of the time-domain evolution of solutions. The finite element time-domain (FETD) techniques that are already prevalent in modeling such structures can readily incorporate the new developments we are offering in this article. We are actively pursuing such issues in our current research.

Chapter 4

Acknowledgments

I would like to thank Professor L. R. Ram-Mohan for his guidance and support in every phase of this project. In addition, I would like to thank Cody Ah-Heng, who laid the groundwork for many of the FEM codes used to analyze waveguides in preparation for this project; Paul Kassebaum, who provided invaluable help, especially in the creation of vibrant visualization tools for the solutions presented here, and in the use of group representation theory to explain the behavior of the photonic crystal eigenfunctions; and Andrei Ilyashenko, for his experience and useful advice concerning computational issues. Furthermore, I would like to thank Dr. J. D. Albrecht for his constant support, and the benefit of his experience.

Bibliography

[1] L. R. Ram-Mohan, *Finite Element and Boundary Element Applications in Quantum Mechanics* (Oxford, New York, 2002).

[2] K. Bell, *A refined triangular plate bending finite element*, International Journal for Numerical Methods in Engineering, **1**, 101–122 (1969). Also see, I. Holand and K. Bell, *Finite Element Methods in Stress Analysis* (Tapir, Trondheim, 1970).

[3] J. H. Argyris, I. Fried, D. W. Scharpf, *The TUBA Family of Plate Elements for the Matrix Displacement Method*, Imperial College of Science and Technology, University of London, Technical Note 14, 701–709 (1968).

[4] Gouri Dhatt and Gilbert Touzot, *The Finite Element Method Displayed*, (John Wiley & Sons, April 1984)

[5] P. G. Kassebaum, C. R. Boucher, L. R. Ram-Mohan, *Application of Group Representation Theory to Derive Hermite Interpolation Polynomials on a Triangle*, Journal of Computational Physics, to appear (2012).

[6] M. S. Dresselhaus, G. Dresselhaus, A. Jorio, *Group Theory: Application to the Physics of Condensed Matter*, (Springer, Berlin, Germany, 2008).

[7] M. Israel and R. Miniowitz, *An Efficient Finite Element Method for Nonconvex Waveguide Based on Hermitian Polynomials*, IEEE Trans. Microwave Theory Tech. MTT-**35**, 1019–1025 (1987).

[8] M. Israel and R. Miniowitz. *Hermitian finite-element method for inhomogeneous waveguides*, IEEE Trans. Microwave Theory Tech. **38**, 1319–1327 (1990).

[9] E. Yablonovitch, *Inhibited Spontaneous Emission in Solid-State Physics and Electronics*, Phys. Rev. Lett. **58**, 2059–2062 (1987).

[10] S. John, *Strong localization of photons in certain disordered dielectric superlattices*, Phys. Rev. Lett. **58**, 2486–2489 (1987).

[11] S. G. Johnson, J. D. Joannopoulos, *Photonic Crystals: The Road from Theory to Practice* (Kluwer, Massachusetts, 2002).

[12] K. Ohtaka and M. Inoue, *Energy band of photons and low-energy photon diffraction*, Phys. Rev. B **19**, 5057–5067 (1979).

[13] K. Sakoda, *Symmetry, degeneracy, and uncoupled modes in two-dimensional photonic lattices*, Phys. Rev. B **52**, 7982-7986 (1995).

[14] K. Sakoda, *Group-theoretical classification of eigenmodes in three-dimensional photonic lattices* Phys. Rev. B **55**, 15345-15348 (1997).

[15] K. Sakoda, *Optical Properties of Photonic Crystals* (Springer, Berlin, Germany, 2001).

[16] J.B. Pendry, *Photonic Band Structures*, Journal of Modern Optics, **41:2**, 209–229, 1994.

[17] H. Benisty, V. Berger, J.-M Gérard, D. Maystre, A. Tchelnokov, *Photonic Crystals: Towards Nanoscale Photonic Devices* (Springer, Berlin, Germany, 2005).

[18] F. Bloch, *Über die quantenmechanik der electronen in kristallgittern*, Zietshrift der Physik **52**, 555-600 (1928).

[19] G. Floquet, *Sur les équations différentielles linéaries à coefficients périodiques*, Annales de l'École Normale Supérieure **12** 47-88 (1883).

[20] C. Kittel, *Introduction to Solid State Physics* (John Wiley & Sons, New York, 2005).

[21] D. S. Jones, *The Theory of Electromagnetism* (Macmillan, New York, 1964).

[22] J. D. Joannopoulos, S. G. Johnson, J. N. Winn, R. D. Meade, *Photonic Crystals: Molding the Flow of Light, 2nd ed.* (Princeton, New Jersey, 2008).

[23] Z. J. Cendes, *Unlocking the magic of Maxwells equations* IEEE Spectrum **26**, 29–33 (1989).

[24] V. G. Veselago *The electrodynamics of substances with simultaneously negative values of* ϵ *and* μ, Soviet Phys. Usp. 10, 509–514 (1968) [Usp. Fiz. Nauk 92, 517–526 (1967).

[25] J. B. Pendry, *Negative Refraction Makes a Perfect Lens*, Physical Review Letters **85** 3966-3969 (2000).

[26] D. R. smith, Willie J. Padilla, D. C. Vier, S. C. Nemat-Nasser and S. Schultz, *A Composite medium with simultaneously negative permeability and permittivity*, Physical Review Letters **84**, 4184–4187 (2000).